Metabolic regulation of misfolded protein import into mitochondria

Authors: Yuhao Wang[1,2†], Linhao Ruan[1†], Jin Zhu[3], Xi Zhang[1], Alexander Chih-Chieh Chang[1,4], Alexis Tomaszewski[1,2], Rong Li[1,3,4*]

Affiliations:

[1]Center for Cell Dynamics and Department of Cell Biology, Johns Hopkins University School of Medicine; Baltimore, MD 21205, USA.

[2]Biochemistry, Cellular and Molecular Biology (BCMB) Graduate Program, Johns Hopkins University School of Medicine; Baltimore, MD 21287, USA.

[3]Mechanobiology Institute and Department of Biological Sciences, National University of Singapore; Singapore 117411, Singapore.

[4]Department of Chemical and Biomolecular Engineering, Whiting School of Engineering, Johns Hopkins University; Baltimore, MD 21218, USA.

†These authors contributed equally to this work

* Corresponding author. Email: rong@jhu.edu

Abstract

Mitochondria are the cellular energy hub and central target of metabolic regulation. Mitochondria also facilitate proteostasis through pathways such as the 'mitochondria as guardian in cytosol' (MAGIC) whereby cytosolic misfolded proteins (MPs) are imported into and degraded inside mitochondria. In this study, a genome-wide screen in yeast uncovered that Snf1, the yeast AMP-activated protein kinase (AMPK), inhibits the import of MPs into mitochondria while promoting mitochondrial biogenesis under glucose starvation. We show that this inhibition requires a downstream transcription factor regulating mitochondrial gene expression and is likely to be conferred through substrate competition and mitochondrial import channel selectivity. We further show that Snf1/AMPK activation protects mitochondrial fitness in yeast and human cells under stress induced by MPs such as those associated with neurodegenerative diseases.

Introduction

Mitochondria are vital organelles whose biogenesis and activities in energy production are tightly linked to cellular metabolic control (*1*,*2*). Metabolic stress and mitochondrial dysfunction are common drivers of age-related degenerative diseases such as heart failure and dementia (*3*,*4*), which are often characterized by loss of proteostasis leading to the formation of protein aggregates (*3*,*5*). In yeast, acute proteotoxic stress such as heat shock induces reversible protein aggregation in cytosol (*6*-*10*). Protein aggregates are initially formed on the cytosolic surface of the endoplasmic reticulum (ER), and later captured at the mitochondrial outer membrane (*7*,*8*). Upon reversal to the stress-free condition, aggregates undergo dissolution that is not only dependent on the activity of the Hsp104 chaperone but also mitochondrial membrane potential (*8*,*10*). This observation led to a hypothesis that mitochondria play an active role in the clearance of cytosolic MPs. Using both imaging-based as well as biochemical assays, we showed that certain aggregation-prone native cytosolic proteins and the model aggregation protein firefly luciferase

single mutant (FlucSM) (*11*), but not stable cytosolic proteins, are imported into the mitochondrial matrix (*10*). A subset of highly aggregation-prone proteins known as super-aggregators (*9*) are imported into mitochondria even in the absence of heat stress (*10*). Mitochondrial proteases, most prominently the LON protease Pim1, degrade the imported MPs in the mitochondrial matrix, and this pathway of clearance of cytosolic MPs was termed 'mitochondria as guardian in cytosol' (MAGIC) (*10*) (Figure 1—figure supplement 1A).

Cytosolic MPs have also been found in human mitochondria. Both FlucSM and a more destabilized double mutant (FlucDM) (*11*), but not the well-folded wild-type Fluc (FlucWT) or glutathione S-transferase (GST), are imported into the mitochondrial matrix of human RPE-1 cells (*10*). In HeLa cells, proteasomal inhibition by MG132 induces the mitochondrial import of unfolded cytosolic model protein in a manner dependent on mitochondrial outer membrane protein FUNDC1 and cytosolic chaperone HSC70 (*12*). Furthermore, disease-related proteins such as α-synuclein (αSyn), FUS, and TDP-43 are found in the mitochondria of human cells (*13-15*). These results suggest that a MAGIC-like pathway may exist in higher organisms, although the underlying mechanisms could be different.

It remains unclear whether MAGIC is beneficial or detrimental to cellular or mitochondrial fitness. Nevertheless, the MAGIC pathway may represent a link between mitochondrial dysfunction and loss of proteostasis. Although inhibition of mitochondrial import after heat shock causes prolonged protein aggregation in cytosol, an elevated burden of MPs in mitochondria can also cause mitochondrial damage (*16*). Understanding how mitochondria balance functions in proteostasis and metabolism may provide key insights into the maintenance of cellular fitness under stress during aging. In this work, we conducted an unbiased imaging-based genetic screen in yeast to uncover cellular mechanisms that regulate MAGIC. We identified Snf1, the yeast AMP-activated kinase (AMPK), as a negative regulator of MAGIC through transcriptional upregulation of nuclear-encoded mitochondrial genes. We also showed that AMPK activation in yeast and human cells attenuates mitochondrial accumulation of disease-related MPs and may protect cellular fitness under proteotoxic stresses.

Results

A genetic screening for regulators of MAGIC

To observe the mitochondrial import of cytosolic MPs, we employed a previously established method using split-GFP (spGFP) system in which the first ten β-strand of GFP (GFP_{1-10}) was targeted into the mitochondrial matrix while the eleventh β-strand (GFP_{11}) was tagged with MPs (*10*) (Figure 1—figure supplement 1B). Because mitochondrial import requires substrate in an unfolded state (*17*), globular GFP reconstituted in the cytosol should not be imported. Indeed, mitochondrial spGFP signal of stable cytosolic protein Hsp104 failed to increase after heat shock (*10*) (Figure 1—figure supplement 1C). In contrast, spGFP signals of FlucSM and several endogenous aggregation-prone proteins increased significantly after heat shock at 42 °C compared to background at normal growth temperature (30 °C) in wild-type cells (*10*). Importantly, mitochondrial import of FlucSM and other misfolded cytosolic proteins after heat stress was further validated by using a variety of additional methods, including the classical biochemical fractionation and protease protection assay, APEX-based labeling in mitochondrial matrix, and super-resolution microscopy (*10*).

To uncover cellular pathways that influence MAGIC, we performed a high-throughput spGFP-based genetic screen in the non-essential yeast knockout (YKO) collection (*18*) (Figure 1A). Briefly, for each mutant strain in this collection, Lsg1, one of the endogenous aggregation-prone proteins previously shown to be imported into mitochondria (*10*), was C-terminally tagged with GFP_{11} at *LSG1* genomic locus through homologous recombination. Also introduced into each mutant strain was a construct constitutively expressing matrix targeted GFP_{1-10} under the GAPDH promoter. GFP_{1-10} was targeted into mitochondrial matrix by using the cleavable mitochondrial targeting sequence (MTS) of Subunit 9 of mitochondrial ATPase (Su9) from *Neurospora crassa*, and the red fluorescent protein mCherry was also included in this construct (MTS-mCherry-GFP_{1-10}), as previously described (*10*). YKO mutants bearing the above Lsg1 spGFP reporter components were generated by using high-throughput transformation in 96-well plates. We used flow cytometry and analyzed Lsg1 spGFP signal of each mutant at 30 °C and after 42 °C heat shock for 30 min (Figure 1—figure supplement 1D). Mutants of interest were then subjected to

hits validation using confocal fluorescence imaging. Based on mitochondrial spGFP intensity of each mutant and wild-type (WT) cells at two imaging time points, we classified the validated YKO mutants into two groups: five Class 1 mutants showed significant greater spGFP signal than WT at 30 °C without heat shock, and 140 Class 2 mutants had no significant increase in spGFP signal after heat stress compared to 30 °C (Table S1; Details in Materials and Methods).

KEGG pathway analysis revealed that genes corresponding to the hits validated with imaging encompassed many cellular pathways, most notably carbohydrate metabolism and ribosomal biogenesis (Figure 1B). Among five Class 1 mutants, a notable one is *Δsnf1* (Figure 1C and D; See further analyses below). Class 2 includes multiple genes related to ribosomal biogenesis (Table S1). For example, deletion of *LTV1* that encodes a chaperone required for the assembly of small ribosomal subunits (*19*) showed only baseline level Lsg1 spGFP fluorescence with no increase at 42 °C (Figure 1E and F).

Snf1/AMPK negatively regulates MP accumulation in mitochondria

In this study, we have chosen to focus on *SNF1*, as *SNF1* encodes the yeast homolog of the evolutionarily conserved AMPK which serves as a master nutrient sensor orchestrating the activation of glucose-repressed gene transcription and metabolic stress response in glucose-limited conditions (*20-22*). Its pivotal function in cellular metabolism and mitochondrial biogenesis spurred us to further examine its role in MAGIC. To avoid complicating effects of heat shock and to improve the sensitivity of spGFP reporter, we optimized our spGFP-based method to impose proteostasis burden by acute induction of the MAGIC substrate FlucSM (*10,11*) tagged with GFP_{11} (FlucSM-GFP_{11}) via the β-estradiol-inducible system (*23*). GFP_{1-10} was stably targeted to the mitochondrial matrix by fusion with a matrix protein Grx5 (Grx5-GFP_{1-10}). After induction upon β-estradiol treatment at 30 °C for 90 min, FlucSM spGFP signal increased significantly within mitochondria compared to the ethanol-treated control (Figure 1G and H; Figure 1—figure supplement 2A-C; Movie S1). The spGFP signal in mitochondria showed an increasing trend that positively correlated with the structural instability of luciferase-derived MPs: FlucWT, FlucSM, and FlucDM with the highest structural instability (*11*) (Figure 1—figure supplement 2D and E).

We chose to use the intermediate construct, FlucSM-GFP$_{11}$, for testing the effects of modulating Snf1 activity on mitochondrial import of MPs.

Reg1 is the regulatory subunit of Glc7-Reg1 protein phosphatase 1 complex that dephosphorylates Snf1 and promotes its inhibitory conformation (*24-27*). Either glucose limitation or loss of Reg1 in glucose-rich medium (HG: 2% glucose) result in constitutive activation of Snf1 and relief from glucose repression of transcription (*24-28*) (Figure 1I). We found that *Δreg1* cells exhibited significantly less accumulation of FlucSM in mitochondria than WT cells, and likewise, wild-type cells that grew in low glucose medium (LG: 0.1% glucose plus 3% glycerol) showed significantly lower FlucSM spGFP compared to cells in HG (Figure 1G and H). The absence of glycerol in LG (LG-Gly) did not cause any noticeable difference to LG (Figure 1—figure supplement 2F and G). Snf1 activation under these conditions was validated by the nuclear export of Mig1, which depends on phosphorylation by active Snf1 (*29-31*) (Figure 1—figure supplement 2H and I). In addition, the abundance of FlucSM-GFP$_{11}$ induced by estradiol was not affected by Snf1 activation, and Grx5-GFP$_{1-10}$ level was unchanged in low glucose media and even elevated in *Δreg1* cells - a trend opposite of the spGFP changes (Figure 1—figure supplement 2J). These data exclude the possibility that reduced expression of either protein led to lower spGFP signal in mitochondria. To examine the effect of Snf1 activation on spGFP reconstitution, Grx5 spGFP strain was constructed in which the endogenous mitochondrial matrix protein Grx5 was C-terminally tagged with GFP$_{11}$ at its genomic locus, and GFP$_{1-10}$ was targeted to mitochondria through cleavable Su9 MTS (MTS-mCherry-GFP$_{1-10}$) (*10*). Only modest reduction in Grx5 spGFP mean intensity was observed in LG compared to HG, and no significant difference after adjusting the GFP$_{1-10}$ abundance (spGFP/mCherry ratio) (Figure 1—figure supplement 3A-D). These data suggest that any effect on spGFP reconstitution is insufficient to explain the drastic reduction of MP accumulation in mitochondria under Snf1 activation. Overall, our results demonstrate that Snf1 activation primarily prevents mitochondrial accumulation of MPs, but not that of normal mitochondrial proteins.

We previously showed that the import of firefly luciferase mutants into mitochondria of human RPE-1 cells was positively correlated with protein instability (*10,11*). Using the established spGFP reporter, we found that treatment of RPE-1 cells with dorsomorphin, a chemical inhibitor of AMPK (*32*), significantly increased mitochondrial accumulation of FlucDM (Figure 1J and K), but not GST, a well-folded protein control (Figure 1L). In contrast, pharmacological activation of

AMPK via 5-aminoimidazole-4-carboxamide ribonucleoside (AICAR) (*33*), significantly reduced FlucDM accumulation in mitochondria (Figure 1J and M). These results suggest that AMPK in human cells regulates MP accumulation in mitochondria following a similar trend as in yeast, although the underlying mechanisms might differ between these organisms.

Mechanisms of MAGIC regulation by Snf1

The accumulation of MPs in mitochondria as observed using the spGFP reporter should depend on the relative rates of import versus degradation by mitochondrial proteases, most prominently Pim1 – the conserved Lon protease in yeast (*10*). Three possible factors could therefore contribute to the reduced mitochondrial accumulation of MPs under Snf1 activation: 1) enhanced intra-mitochondrial degradation, 2) reduced cytosolic misfolded protein (due to enhanced folding and/or other degradation pathways), and 3) blocked mitochondrial import (Figure 2A). To evaluate the first possibility, an antimorphic mutant *pim1*^{S974D} was used to block the degradation of imported FlucSM in the mitochondrial matrix (*34*). Indeed, in HG medium wild-type cells overexpressing *pim1*^{S974D} showed a significantly increased accumulation of FlucSM in mitochondria compared to cells overexpressing *PIM1* (Figure 2B and C). However, *pim1*^{S974D} overexpression was unable to increase FlucSM accumulation in mitochondria of *Δreg1* cells or WT cells growing in LG medium (Figure 2B and C). This result argued against the first possibility, and consistently the abundance of Pim1 protein was not increased by switching to nonfermentable carbon sources (*35*). To evaluate the second possibility, we used an *in vivo* firefly luciferase assay (*36*) and assessed the folding of enzymatically active FlucSM after estradiol induction. The result showed that Snf1-active cells exhibited reduced FlucSM luciferase activity, suggesting an increased rather than decreased fraction of misfolded FlucSM (Figure 2D). Furthermore, blocking the activated autophagy pathway in LG medium (*37*) did not increase FlucSM spGFP in mitochondria (Figure 2—figure supplement 1A and B). We also observed that proteasomal inhibition through MG132 treatment stimulated the mitochondrial accumulation of FlucSM but did not ablate the difference between HG and LG condition (Figure 2—figure supplement 1C). The stimulating effect of MG132 was not surprising because FlucSM is degraded by proteasome in the cytosol (*10*) and preventing this pathway could divert more of such protein molecules toward MAGIC. We thus

favor the third possibility that Snf1 activation specifically prevents the import of MPs into mitochondria.

Next, we investigated downstream transcription factors that could mediate the Snf1-regulated MP import (Figure 2E). In the presence of abundant glucose and when Snf1 activity is low, transcriptional repressor Mig1 and its partially redundant homolog Mig2 are localized in the nucleus to confer glucose-repressed gene expression (*29-30, 38*). However, neither single deletion of *MIG1* nor double deletions of *MIG1* and *MIG2* reduced FlucSM spGFP in HG medium (Figure 2—figure supplement 1D and E), suggesting that Mig1 and/or Mig2-repressed gene expression was not sufficient to prevent MP import (Figure 2E, left branch). Then we tested if MP import was antagonized by transcriptional activators downstream of Snf1 including Cat8, Hap4, Sip4, Adr1 and Rds2 (*21, 39-41*) (Figure 2E, right branch). Interestingly, only deletion of *HAP4*, but not other transcriptional activators, significantly rescued FlucSM import defect in *Δreg1* cells with Snf1 activation (Figure 2F and G; Figure 2—figure supplement 1F and G). When cultured in LG medium, *HAP4* deletion also resulted in a significant increase in mitochondrial accumulation of FlucSM in comparison to WT (Figure 2—figure supplement 1H). Furthermore, overexpression of Hap4 alone was sufficient to reduce FlucSM spGFP in HG medium (Figure 2H and I). These data suggest that Hap4 is a main downstream effector of Snf1 that regulates MP import.

Hap4 is the transcriptional activation subunit in the Hap2/3/4/5 complex that activates the expression of nuclear encoded mitochondrial proteins and contributes to mitochondrial biogenesis during metabolic shifts or cellular aging (*39-43*). We hypothesized that elevated expression of mitochondrial preprotein induced by activation of Snf1-Hap4 axis (*20,35,43-46*) may outcompete MPs for import channels, especially considering that the expression of TOM complex components on the mitochondrial outer membrane was static in Snf1-active cells (*35,46*) (Figure 3A).

To test this hypothesis, we attempted to restore MP import during Snf1 activation by using high-level expression of the soluble cytosolic domain of import receptors. The cytosolic import receptors lacking membrane-anchoring sequences are known to prevent mitochondrial preproteins from binding TOM complexes and thus inhibit preprotein import (*47-49*) (Figure 3—figure supplement 1A). Interestingly, overexpression of the cytosolic domain of Tom70 ($Tom70_{cd}$), but not $Tom20_{cd}$ or $Tom22_{cd}$, significantly increased FlucSM import in LG medium (Figure 3B and

C). $Tom70_{cd}$ also further increased FlucSM import in HG medium (Figure 3—figure supplement 1B and C). The effect of $Tom70_{cd}$ in cytosol required both the substrate binding and the chaperone-interaction domain (Figure 3C; Figure 3—figure supplement 1D and E). These results suggest that Tom70-dependent preprotein import may compete with misfolded protein import for limited TOM complexes. To further test if endogenous full-length Tom70 on the mitochondrial outer membrane is dispensable for MP import, we deleted *TOM70* and its paralog *TOM71* and found that in HG medium where mitochondrial respiration is not essential, FlucSM accumulation in mitochondria was not impaired in single mutants and increased in double mutant (Figure 3D and E). This result indicates that MP import does not use Tom70/Tom71 as obligatory receptors. The effect of *Δtom70Δtom71* on MP import was consistent, albeit less pronounced, with $Tom70_{cd}$ overexpression (Figure 3D and E; Figure 3—figure supplement 1B and C). One potential explanation for the modest effect in double mutant is that given to the functional redundance between Tom20 and Tom70 (*50,51*), Tom20 receptors in *Δtom70Δtom71* cells could instead mediate preprotein import, whereas cytosolic $Tom70_{cd}$ may have a dominant inhibitory effect on preprotein import by reducing association between preproteins and mitochondrial outer membrane or TOM complexes (*47-49*). Together, these data suggest that increased expression and receptor-dependent import of certain mitochondrial preproteins under Snf1 activation might indirectly restrict the import of MPs.

As the main entry gate for mitochondrial preproteins, the TOM complex adopts two functional conformations with different substrate specificity: the receptor-free dimer is primarily responsible for importing MIA pathway substrates, and the receptor-bound trimer for Tim23 pathway substrates (*52-54*). Deletion of Tom6 disassembles the trimer and shifts the conformation equilibrium toward the dimer form (*54,55*). To test if the substrate selectivity of TOM complex regulates MP import, we eliminated the trimer conformation by deleting *TOM6* and found that it elevated FlucSM import in LG medium with or without $Tom70_{cd}$ overexpression (Figure 3F and G; Figure 3—figure supplement 1F and G). This result suggests that restricting MP import under Snf1 activation requires the trimeric TOM complex in addition to the competing mitochondrial preprotein import, and MPs might preferentially cross the mitochondrial outer membrane through the dimeric TOM complex.

AMPK protects cellular fitness during proteotoxic stress

We next investigated the physiological effects of metabolic regulation of MAGIC mediated by Snf1/AMPK. Prolonged induction of high-level FlucSM expression imposed a proteotoxic stress and led to a reduced growth rate in HG medium compared to the control, but interestingly no growth reduction was observed under glucose limitation (Figure 4A; Figure 4—figure supplement 1A, D and E). We reasoned that the lack of growth defect in LG medium could be due to prevention of MP import into mitochondria downstream of Snf1 activation. Supporting this, elevating MP import by $Tom70_{cd}$ overexpression led to a reduced growth rate in LG medium that was dependent on FlucSM expression (Figure 4A; Figure 4—figure supplement 1B). $Tom70_{cd}$ overexpression also exacerbated growth rate reduction due to FlucSM expression in HG medium (Figure 4A; Figure 4—figure supplement 1B). In contrast, negative controls using truncated $Tom70_{cd}$ mutants that could not restore MP import did not produce the same growth defect (Figure 4—figure supplement 1C).

To further test whether the reduction in growth rate during proteotoxic stress was associated with impaired mitochondrial fitness, we assessed mitochondrial membrane potential (MMP) using the dye tetramethylrhodamine methyl ester (TMRM). In HG medium and after 90 min induction of FlucSM, there was a negative relationship between spGFP accumulation and MMP: spGFP-positive cells exhibited a significantly reduced MMP level than spGFP-negative cells (Figure 4C). Again, this difference was not observed in cells that grew in LG, whereas $Tom70_{cd}$ overexpression led to a significant increase in the fraction of spGFP-positive cells with reduced MMP in both HG and LG medium (Figure 4B and C). These results suggest that Snf1 activation under glucose limitation protects mitochondrial and cellular fitness from FlucSM-associated proteotoxic stress.

Many neurodegenerative disease-associated aggregation-prone proteins, such as α-synuclein (*13*), FUS^{P525L} (*14*,*56*), TDP-43 (*15*), amyloid beta (*57*), and C9ORF72-associated poly(GR) dipeptide (*58*), are detected in mitochondria of human patients or disease models and impair mitochondrial functions. We wonder whether such toxic effects of disease-associated proteins can be counteracted by AMPK activation. First, we used the spGFP reporter in yeast and observed mitochondrial import of α-synuclein and FUS^{P525L} in HG medium (Figure 4D and 4E; Figure 4—figure supplement 1F and G; Movie S2). We found that Snf1 activation via glucose limitation or

Δreg1 significantly reduced their accumulation in mitochondria, whereas $Tom70_{cd}$ overexpression reversed this effect (Figure 4D-I; Figure 4—figure supplement 1H-K). Mitochondrial import of α-synuclein and FUS^{P525L} in HG medium was associated with lower MMP, and $Tom70_{cd}$ overexpression significantly increased the fraction of spGFP-positive and MMP-low cells in both HG and LG medium (Figure 4J-K). Furthermore, accumulation of α-synuclein in mitochondria correlated with a loss of respiratory capacity, as overexpression of $Tom70_{cd}$ and α-synuclein synergistically promoted the formation of respiration-deficient petite cells (Figure 4L).

We next tested whether reducing mitochondrial accumulation of FUS^{P525L} ameliorates its cellular toxicity in human cells. FUS^{P525L} has been shown to bind mitochondrial Hsp60 and ATP synthase β-subunit to induce mitochondrial fragmentation and cell death (*14,56*). We expressed FUS^{P525L} into human RPE-1 cells by transient transfection and confirmed the import of FUS^{P525L} into mitochondrial matrix using the spGFP reporter (Figure 5A and B). FUS^{P525} expression also caused the loss of MMP and elevated cell death compared to GST control (Figure 5C and D). Importantly, mitochondrial accumulation and fitness decline caused by FUS^{P525} expression were significantly reduced by activation of AMPK via AICAR treatment (Figure 5B-D). These results suggest a protective role of AMPK in FUS-induced cellular toxicities possibly through preventing the import of the disease protein into mitochondria.

Discussion

Metabolic imbalance and loss of proteostasis are interconnected hallmarks of aging and age-related diseases (*3,5,59*). Various metabolic signaling pathways, such as TOR, AMPK, Sirtuins, and insulin/IGF-1, sense metabolic stimuli, regulate cellular stress responses and influence major cytosolic protein quality control mechanisms including ubiquitin-proteasome pathway and autophagy (*59*). Mitochondria, the central target of metabolic signaling and major hub of energy production, participate in proteostasis by importing of cytosolic misfolded proteins lacking canonical mitochondrial targeting sequences via the MAGIC pathway (*10*). Here, our unbiased genetic screen in yeast revealed an unexpected link between cellular metabolism and proteostasis

through MAGIC. Our data established Snf1/AMPK as a key regulator of misfolded protein import, which balances the mitochondrial metabolic and proteostasis functions in response to glucose availability and protects mitochondrial fitness under proteotoxic stress (Figure 5E). We speculate that, when glucose level is high and cells rely on glycolysis for ATP production, mitochondria play a 'moonlighting role' in cellular proteostasis through MAGIC, a process dependent on mitochondrial import and proteostasis machineries including chaperones, mitochondrial translocons, and proteases (*10*). On the other hand, when glucose is limited and cells rely on oxidative phosphorylation for ATP generation, Snf1/AMPK activation shuts down MAGIC and promotes import of essential mitochondrial preproteins, thus ensuring mitochondrial fitness and energy production.

The downstream mechanism of this regulation remains to be fully elucidated. We propose that in yeast Snf1 activates the Hap4-dependent expression of mitochondrial preproteins which could compete with MPs for limited TOM complexes under glucose-limiting condition. Using cytosolic domain of Tom receptors to dampen preprotein import, we showed that only $Tom70_{cd}$ rescued MP import under Snf1 activation. A recent study (*60*) suggests that overexpression of full-length Tom70 leads to transcriptional activation for mitochondrial biogenesis. Whether the cytosolic $Tom70_{cd}$ fragment plays an indirect role in mitochondrial import through transcriptional regulation should be tested in the future. Since Snf1/Hap4 activation elevates the expression of hundreds of mitochondrial preproteins (*35*,*43-46*), it remains to be determined if specific preproteins or cytosolic factors are directly involved in inhibiting MP import. Furthermore, whether this metabolic control of MP import applies to other uncharacterized MAGIC substrates awaits further investigation.

Our data also suggest that the trimeric form of the TOM complex maintained by Tom6 is important for limiting MP entry under glucose restriction. We speculate that the receptor-binding state and substrate selectivity of different TOM conformations (*54*) could affect the permeability for MPs to enter mitochondria. Existing proteomic data suggest that the abundance of Tom6 is unaffected by Snf1 activation (*35*) (Figure 3A). As Tom6 can be phosphorylated by Cdk1 in a cell-cycle dependent manner (*55*), it may be interesting to investigate if Tom6 or other TOM complex components are targets of Snf1 kinase activity to directly modulate substrate specificity of the TOM complex.

A question raised by our findings is whether MAGIC is beneficial or detrimental to cells. Our data suggest that under physiological stress-free conditions, MP import and degradation in mitochondria is well-tolerated, but an acute or chronic increase in the cytosolic misfolded protein load could overwhelm mitochondrial proteostasis capacity leading to organellar damage. If so, the regulation of MAGIC by AMPK could help explain the beneficial effect of caloric restriction on life span extension in model organisms (*43*,*61*). In humans, the role of AMPK in health and diseases is complex and not fully understood (*62*-*64*). While AMPK activity and mitochondrial gene expression mediated by downstream transcriptional factors such as PGC-1α and FOXO are elevated during health-benefitting activities such as exercise (*64*), hyperactivated AMPK has also been reported in several neurodegenerative diseases with proteostasis decline (*62*). Our findings suggest that elevating AMPK activity may be beneficial for alleviating proteotoxicity associated with degenerative diseases. Further studies using genetic approaches and relevant *in vivo* models could help elucidate the physiological role of AMPK in balancing proteostasis and mitochondrial fitness.

References:

1. C. Andréasson, M. Ott, S. Büttner, Mitochondria orchestrate proteostatic and metabolic stress responses. *EMBO Rep*. **20**, e47865 (2019).

2. T. Wai, T. Langer, Mitochondrial Dynamics and Metabolic Regulation. *Trends Endocrinol Metab*. **27**, 105–117 (2016).

3. C. López-Otín, M. A. Blasco, L. Partridge, M. Serrano, G. Kroemer, Hallmarks of aging: An expanding universe. *Cell*. **186**, 243–278 (2023).

4. J. Nunnari, A. Suomalainen, Mitochondria: in sickness and in health. *Cell*. **148**, 1145–1159 (2012).

5. M. S. Hipp, P. Kasturi, F. U. Hartl, The proteostasis network and its decline in ageing. *Nat Rev Mol Cell Biol*. **20**, 421–435 (2019).

6. C. Zhou, B. D. Slaughter, J. R. Unruh, A. Eldakak, B. Rubinstein, R. Li, Motility and Segregation of Hsp104-Associated Protein Aggregates in Budding Yeast. *Cell*. **147**, 1186–1196 (2011).

7. S. Escusa-Toret, W. I. M. Vonk, J. Frydman, Spatial sequestration of misfolded proteins by a dynamic chaperone pathway enhances cellular fitness during stress. *Nat Cell Biol*. **15**,

1231–1243 (2013).

8. C. Zhou, B. D. Slaughter, J. R. Unruh, F. Guo, Z. Yu, K. Mickey, A. Narkar, R. T. Ross, M. McClain, R. Li, Organelle-Based Aggregation and Retention of Damaged Proteins in Asymmetrically Dividing Cells. *Cell*. **159**, 530–542 (2014).

9. E. W. J. Wallace, J. L. Kear-Scott, E. V. Pilipenko, M. H. Schwartz, P. R. Laskowski, A. E. Rojek, C. D. Katanski, J. A. Riback, M. F. Dion, A. M. Franks, E. M. Airoldi, T. Pan, B. A. Budnik, D. A. Drummond, Reversible, Specific, Active Aggregates of Endogenous Proteins Assemble upon Heat Stress. *Cell*. **162**, 1286–1298 (2015).

10. L. Ruan, C. Zhou, E. Jin, A. Kucharavy, Y. Zhang, Z. Wen, L. Florens, R. Li, Cytosolic proteostasis through importing of misfolded proteins into mitochondria. *Nature*. **543**, 443–446 (2017).

11. R. Gupta, P. Kasturi, A. Bracher, C. Loew, M. Zheng, A. Villella, D. Garza, F. U. Hartl, S. Raychaudhuri, Firefly luciferase mutants as sensors of proteome stress. *Nat Methods*. **8**, 879–884 (2011).

12. Y. Li, Y. Xue, X. Xu, G. Wang, Y. Liu, H. Wu, W. Li, Y. Wang, Z. Chen, W. Zhang, Y. Zhu, W. Ji, T. Xu, L. Liu, Q. Chen, A mitochondrial FUNDC1/HSC70 interaction organizes the proteostatic stress response at the risk of cell morbidity. *EMBO J*. **38**, e98786 (2019).

13. L. Devi, V. Raghavendran, B. M. Prabhu, N. G. Avadhani, H. K. Anandatheerthavarada, Mitochondrial Import and Accumulation of α-Synuclein Impair Complex I in Human Dopaminergic Neuronal Cultures and Parkinson Disease Brain. *Journal of Biological Chemistry*. **283**, 9089–9100 (2008).

14. J. Deng, P. Wang, X. Chen, H. Cheng, J. Liu, K. Fushimi, L. Zhu, J. Y. Wu, FUS interacts with ATP synthase beta subunit and induces mitochondrial unfolded protein response in cellular and animal models. *Proc. Natl. Acad. Sci. U.S.A.* **115** (2018), doi:10.1073/pnas.1806655115.

15. W. Wang, L. Wang, J. Lu, S. L. Siedlak, H. Fujioka, J. Liang, S. Jiang, X. Ma, Z. Jiang, E. L. Da Rocha, M. Sheng, H. Choi, P. H. Lerou, H. Li, X. Wang, The inhibition of TDP-43 mitochondrial localization blocks its neuronal toxicity. *Nat Med*. **22**, 869–878 (2016).

16. L. Ruan, J. T. McNamara, X. Zhang, A. C.-C. Chang, J. Zhu, Y. Dong, G. Sun, A. Peterson, C. H. Na, R. Li, Solid-phase inclusion as a mechanism for regulating unfolded proteins in the mitochondrial matrix. *Sci. Adv.* **6**, eabc7288 (2020).

17. N. Wiedemann, N. Pfanner, Mitochondrial Machineries for Protein Import and Assembly. *Annu. Rev. Biochem.* **86**, 685–714 (2017).

18. G. Giaever, A. M. Chu, L. Ni, C. Connelly, L. Riles, S. Véronneau, S. Dow, A. Lucau-

Danila, K. Anderson, B. André, A. P. Arkin, A. Astromoff, M. El-Bakkoury, R. Bangham, R. Benito, S. Brachat, S. Campanaro, M. Curtiss, K. Davis, A. Deutschbauer, K.-D. Entian, P. Flaherty, F. Foury, D. J. Garfinkel, M. Gerstein, D. Gotte, U. Güldener, J. H. Hegemann, S. Hempel, Z. Herman, D. F. Jaramillo, D. E. Kelly, S. L. Kelly, P. Kötter, D. LaBonte, D. C. Lamb, N. Lan, H. Liang, H. Liao, L. Liu, C. Luo, M. Lussier, R. Mao, P. Menard, S. L. Ooi, J. L. Revuelta, C. J. Roberts, M. Rose, P. Ross-Macdonald, B. Scherens, G. Schimmack, B. Shafer, D. D. Shoemaker, S. Sookhai-Mahadeo, R. K. Storms, J. N. Strathern, G. Valle, M. Voet, G. Volckaert, C. Wang, T. R. Ward, J. Wilhelmy, E. A. Winzeler, Y. Yang, G. Yen, E. Youngman, K. Yu, H. Bussey, J. D. Boeke, M. Snyder, P. Philippsen, R. W. Davis, M. Johnston, Functional profiling of the Saccharomyces cerevisiae genome. *Nature*. **418**, 387–391 (2002).

19. J. C. Collins, H. Ghalei, J. R. Doherty, H. Huang, R. N. Culver, K. Karbstein, Ribosome biogenesis factor Ltv1 chaperones the assembly of the small subunit head. *J Cell Biol*. **217**, 4141–4154 (2018).

20. R. M. Wright, R. O. Poyton, Release of two Saccharomyces cerevisiae cytochrome genes, COX6 and CYC1, from glucose repression requires the SNF1 and SSN6 gene products. *Mol Cell Biol*. **10**, 1297–1300 (1990).

21. K. Hedbacker, M. Carlson, SNF1/AMPK pathways in yeast. *Front Biosci*. **13**, 2408–2420 (2008).

22. D. G. Hardie, AMP-activated/SNF1 protein kinases: conserved guardians of cellular energy. *Nat Rev Mol Cell Biol*. **8**, 774–785 (2007).

23. E. A. Costa, K. Subramanian, J. Nunnari, J. S. Weissman, Defining the physiological role of SRP in protein-targeting efficiency and specificity. *Science*. **359**, 689–692 (2018).

24. J. Tu, M. Carlson, REG1 binds to protein phosphatase type 1 and regulates glucose repression in Saccharomyces cerevisiae. *EMBO J*. **14**, 5939–5946 (1995).

25. K. Ludin, R. Jiang, M. Carlson, Glucose-regulated interaction of a regulatory subunit of protein phosphatase 1 with the Snf1 protein kinase in Saccharomyces cerevisiae. *Proc Natl Acad Sci U S A*. **95**, 6245–6250 (1998).

26. P. Sanz, G. R. Alms, T. A. Haystead, M. Carlson, Regulatory interactions between the Reg1-Glc7 protein phosphatase and the Snf1 protein kinase. *Mol Cell Biol*. **20**, 1321–1328 (2000).

27. A. Ruiz, X. Xu, M. Carlson, Roles of two protein phosphatases, Reg1-Glc7 and Sit4, and glycogen synthesis in regulation of SNF1 protein kinase. *Proc Natl Acad Sci U S A*. **108**, 6349–6354 (2011).

28. M. Caligaris, R. Nicastro, Z. Hu, F. Tripodi, J. E. Hummel, B. Pillet, M.-A. Deprez, J. Winderickx, S. Rospert, P. Coccetti, J. Dengjel, C. De Virgilio, Snf1/AMPK fine-tunes

TORC1 signaling in response to glucose starvation. *Elife*. **12**, e84319 (2023).

29. M. J. De Vit, J. A. Waddle, M. Johnston, Regulated nuclear translocation of the Mig1 glucose repressor. *Mol Biol Cell*. **8**, 1603–1618 (1997).

30. M. A. Treitel, S. Kuchin, M. Carlson, Snf1 protein kinase regulates phosphorylation of the Mig1 repressor in Saccharomyces cerevisiae. *Mol Cell Biol*. **18**, 6273–6280 (1998).

31. M. J. DeVit, M. Johnston, The nuclear exportin Msn5 is required for nuclear export of the Mig1 glucose repressor of Saccharomyces cerevisiae. *Curr Biol*. **9**, 1231–1241 (1999).

32. G. Zhou, R. Myers, Y. Li, Y. Chen, X. Shen, J. Fenyk-Melody, M. Wu, J. Ventre, T. Doebber, N. Fujii, N. Musi, M. F. Hirshman, L. J. Goodyear, D. E. Moller, Role of AMP-activated protein kinase in mechanism of metformin action. *J Clin Invest*. **108**, 1167–1174 (2001).

33. G. Herrero-Martín, M. Høyer-Hansen, C. García-García, C. Fumarola, T. Farkas, A. López-Rivas, M. Jäättelä, TAK1 activates AMPK-dependent cytoprotective autophagy in TRAIL-treated epithelial cells. *EMBO J*. **28**, 677–685 (2009).

34. Nitika, B. Zheng, L. Ruan, J. T. Kline, S. Omkar, J. Sikora, M. Texeira Torres, Y. Wang, J. E. Takakuwa, R. Huguet, C. Klemm, V. A. Segarra, M. J. Winters, P. M. Pryciak, P. H. Thorpe, K. Tatebayashi, R. Li, L. Fornelli, A. W. Truman, Comprehensive characterization of the Hsp70 interactome reveals novel client proteins and interactions mediated by posttranslational modifications. *PLoS Biol*. **20**, e3001839 (2022).

35. M. Morgenstern, S. B. Stiller, P. Lübbert, C. D. Peikert, S. Dannenmaier, F. Drepper, U. Weill, P. Höß, R. Feuerstein, M. Gebert, M. Bohnert, M. van der Laan, M. Schuldiner, C. Schütze, S. Oeljeklaus, N. Pfanner, N. Wiedemann, B. Warscheid, Definition of a High-Confidence Mitochondrial Proteome at Quantitative Scale. *Cell Rep*. **19**, 2836–2852 (2017).

36. D. F. Nathan, M. H. Vos, S. Lindquist, In vivo functions of the Saccharomyces cerevisiae Hsp90 chaperone. *Proc Natl Acad Sci U S A*. **94**, 12949–12956 (1997).

37. R. Iwama, Y. Ohsumi, Analysis of autophagy activated during changes in carbon source availability in yeast cells. *J Biol Chem*. **294**, 5590–5603 (2019).

38. J. O. Westholm, N. Nordberg, E. Murén, A. Ameur, J. Komorowski, H. Ronne, Combinatorial control of gene expression by the three yeast repressors Mig1, Mig2 and Mig3. *BMC Genomics*. **9**, 601 (2008).

39. J. M. Gancedo, Yeast carbon catabolite repression. *Microbiol Mol Biol Rev*. **62**, 334–361 (1998).

40. H.-J. Schüller, Transcriptional control of nonfermentative metabolism in the yeast

Saccharomyces cerevisiae. *Curr Genet*. **43**, 139–160 (2003).

41. J. R. Broach, Nutritional control of growth and development in yeast. *Genetics*. **192**, 73–105 (2012).

42. S. L. Forsburg, L. Guarente, Identification and characterization of HAP4: a third component of the CCAAT-bound HAP2/HAP3 heteromer. *Genes Dev*. **3**, 1166–1178 (1989).

43. S.-J. Lin, M. Kaeberlein, A. A. Andalis, L. A. Sturtz, P.-A. Defossez, V. C. Culotta, G. R. Fink, L. Guarente, Calorie restriction extends Saccharomyces cerevisiae lifespan by increasing respiration. *Nature*. **418**, 344–348 (2002).

44. U. von Plehwe, U. Berndt, C. Conz, M. Chiabudini, E. Fitzke, A. Sickmann, A. Petersen, D. Pfeifer, S. Rospert, The Hsp70 homolog Ssb is essential for glucose sensing via the SNF1 kinase network. *Genes Dev*. **23**, 2102–2115 (2009).

45. V. Hübscher, K. Mudholkar, M. Chiabudini, E. Fitzke, T. Wölfle, D. Pfeifer, F. Drepper, B. Warscheid, S. Rospert, The Hsp70 homolog Ssb and the 14-3-3 protein Bmh1 jointly regulate transcription of glucose repressed genes in Saccharomyces cerevisiae. *Nucleic Acids Res*. **44**, 5629–5645 (2016).

46. F. Di Bartolomeo, C. Malina, K. Campbell, M. Mormino, J. Fuchs, E. Vorontsov, C. M. Gustafsson, J. Nielsen, Absolute yeast mitochondrial proteome quantification reveals trade-off between biosynthesis and energy generation during diauxic shift. *Proc Natl Acad Sci U S A*. **117**, 7524–7535 (2020).

47. J. Brix, K. Dietmeier, N. Pfanner, Differential recognition of preproteins by the purified cytosolic domains of the mitochondrial import receptors Tom20, Tom22, and Tom70. *J Biol Chem*. **272**, 20730–20735 (1997).

48. J. Brix, G. A. Ziegler, K. Dietmeier, J. Schneider-Mergener, G. E. Schulz, N. Pfanner, The mitochondrial import receptor Tom70: identification of a 25 kDa core domain with a specific binding site for preproteins. *J Mol Biol*. **303**, 479–488 (2000).

49. O. Schmidt, A. B. Harbauer, S. Rao, B. Eyrich, R. P. Zahedi, D. Stojanovski, B. Schönfisch, B. Guiard, A. Sickmann, N. Pfanner, C. Meisinger, Regulation of mitochondrial protein import by cytosolic kinases. *Cell*. **144**, 227–239 (2011).

50. H. F. Steger, T. Söllner, M. Kiebler, K. A. Dietmeier, R. Pfaller, K. S. Trülzsch, M. Tropschug, W. Neupert, N. Pfanner, Import of ADP/ATP carrier into mitochondria: two receptors act in parallel. *J Cell Biol*. **111**, 2353–2363 (1990).

51. J. C. Young, N. J. Hoogenraad, F. U. Hartl, Molecular chaperones Hsp90 and Hsp70 deliver preproteins to the mitochondrial import receptor Tom70. *Cell*. **112**, 41–50 (2003).

52. T. Shiota, K. Imai, J. Qiu, V. L. Hewitt, K. Tan, H.-H. Shen, N. Sakiyama, Y. Fukasawa, S. Hayat, M. Kamiya, A. Elofsson, K. Tomii, P. Horton, N. Wiedemann, N. Pfanner, T. Lithgow, T. Endo, Molecular architecture of the active mitochondrial protein gate. *Science*. **349**, 1544–1548 (2015).

53. Y. Araiso, A. Tsutsumi, J. Qiu, K. Imai, T. Shiota, J. Song, C. Lindau, L.-S. Wenz, H. Sakaue, K. Yunoki, S. Kawano, J. Suzuki, M. Wischnewski, C. Schütze, H. Ariyama, T. Ando, T. Becker, T. Lithgow, N. Wiedemann, N. Pfanner, M. Kikkawa, T. Endo, Structure of the mitochondrial import gate reveals distinct preprotein paths. *Nature*. **575**, 395–401 (2019).

54. H. Sakaue, T. Shiota, N. Ishizaka, S. Kawano, Y. Tamura, K. S. Tan, K. Imai, C. Motono, T. Hirokawa, K. Taki, N. Miyata, O. Kuge, T. Lithgow, T. Endo, Porin Associates with Tom22 to Regulate the Mitochondrial Protein Gate Assembly. *Mol Cell*. **73**, 1044-1055.e8 (2019).

55. A. B. Harbauer, M. Opalińska, C. Gerbeth, J. S. Herman, S. Rao, B. Schönfisch, B. Guiard, O. Schmidt, N. Pfanner, C. Meisinger, Mitochondria. Cell cycle-dependent regulation of mitochondrial preprotein translocase. *Science*. **346**, 1109–1113 (2014).

56. J. Deng, M. Yang, Y. Chen, X. Chen, J. Liu, S. Sun, H. Cheng, Y. Li, E. H. Bigio, M. Mesulam, Q. Xu, S. Du, K. Fushimi, L. Zhu, J. Y. Wu, FUS Interacts with HSP60 to Promote Mitochondrial Damage. *PLoS Genet*. **11**, e1005357 (2015).

57. C. A. Hansson Petersen, N. Alikhani, H. Behbahani, B. Wiehager, P. F. Pavlov, I. Alafuzoff, V. Leinonen, A. Ito, B. Winblad, E. Glaser, M. Ankarcrona, The amyloid beta-peptide is imported into mitochondria via the TOM import machinery and localized to mitochondrial cristae. *Proc Natl Acad Sci U S A*. **105**, 13145–13150 (2008).

58. S. Y. Choi, R. Lopez-Gonzalez, G. Krishnan, H. L. Phillips, A. N. Li, W. W. Seeley, W.-D. Yao, S. Almeida, F.-B. Gao, C9ORF72-ALS/FTD-associated poly(GR) binds Atp5a1 and compromises mitochondrial function in vivo. *Nat Neurosci*. **22**, 851–862 (2019).

59. F. Ottens, A. Franz, T. Hoppe, Build-UPS and break-downs: metabolism impacts on proteostasis and aging. *Cell Death Differ*. **28**, 505–521 (2021).

60. Q. Liu, C. E. Chang, A. C. Wooldredge, B. Fong, B. K. Kennedy, C. Zhou, Tom70-based transcriptional regulation of mitochondrial biogenesis and aging. *Elife*. **11**, e75658 (2022).

61. C. L. Green, D. W. Lamming, L. Fontana, Molecular mechanisms of dietary restriction promoting health and longevity. *Nat Rev Mol Cell Biol*. **23**, 56–73 (2022).

62. K. Burkewitz, Y. Zhang, W. B. Mair, AMPK at the nexus of energetics and aging. *Cell Metab*. **20**, 10–25 (2014).

63. G. R. Steinberg, B. E. Kemp, AMPK in Health and Disease. *Physiol Rev*. **89**, 1025–1078

(2009).

64. C. Cantó, L. Q. Jiang, A. S. Deshmukh, C. Mataki, A. Coste, M. Lagouge, J. R. Zierath, J. Auwerx, Interdependence of AMPK and SIRT1 for metabolic adaptation to fasting and exercise in skeletal muscle. *Cell Metab*. **11**, 213–219 (2010).

65. M. S. Longtine, A. McKenzie, D. J. Demarini, N. G. Shah, A. Wach, A. Brachat, P. Philippsen, J. R. Pringle, Additional modules for versatile and economical PCR-based gene deletion and modification in Saccharomyces cerevisiae. *Yeast*. **14**, 953–961 (1998).

66. S. Li, Z. Lavagnino, D. Lemacon, L. Kong, A. Ustione, X. Ng, Y. Zhang, Y. Wang, B. Zheng, H. Piwnica-Worms, A. Vindigni, D. W. Piston, Z. You, Ca2+-Stimulated AMPK-Dependent Phosphorylation of Exo1 Protects Stressed Replication Forks from Aberrant Resection. *Mol Cell*. **74**, 1123-1137.e6 (2019).

67. G. Robert, I. Ben Sahra, A. Puissant, P. Colosetti, N. Belhacene, P. Gounon, P. Hofman, F. Bost, J.-P. Cassuto, P. Auberger, Acadesine kills chronic myelogenous leukemia (CML) cells through PKC-dependent induction of autophagic cell death. *PLoS One*. **4**, e7889 (2009).

68. J. B. Kelley, B. M. Paschal, Fluorescence-based quantification of nucleocytoplasmic transport. *Methods*. **157**, 106–114 (2019).

69. K. L. Witkin, Y. Chong, S. Shao, M. T. Webster, S. Lahiri, A. D. Walters, B. Lee, J. L. Y. Koh, W. A. Prinz, B. J. Andrews, O. Cohen-Fix, The budding yeast nuclear envelope adjacent to the nucleolus serves as a membrane sink during mitotic delay. *Curr Biol*. **22**, 1128–1133 (2012).

70. M. Kahm, G. Hasenbrink, H. Lichtenberg-Fraté, J. Ludwig, M. Kschischo, **grofit** : Fitting Biological Growth Curves with *R*. *J. Stat. Soft.* **33** (2010), doi:10.18637/jss.v033.i07.

71. M. Ogur, R. St. John, S. Nagai, Tetrazolium overlay technique for population studies of respiration deficiency in yeast. *Science*. **125**, 928–929 (1957).

Acknowledgments: We thank C. Zhou and S. Claypool for valuable discussion.

Funding:

National Institutes of Health grant R35 GM118172 (RL)

ReStem Biotech grant (RL)

American Heart Association and DC Women's Board Predoctoral Fellowship AHA 17PRE33670517 (LR)

Isaac Morris Hay and Lucille Elizabeth Hay Graduate Fellowship from Johns Hopkins Cell Biology (LR)

National Institutes of Health grant to BCMB graduate program at Johns Hopkins School of Medicine T32 GM007445 (YW, LR, AT)

Author Contributions:

Conceptualization: YW, LR, RL

Methodology: YW, LR, JZ, AC-CC, XZ, AT

Investigation: YW, LR, RL

Visualization: YW, LR

Writing: YW, LR, JZ, RL

Supervision: RL

Funding acquisition: RL

Competing Interests:

The authors declare no competing interests.

Data and materials availability:

All data needed to evaluate the conclusions are available in the main text or the supplementary materials. Additional data and materials related to this study can be requested from the authors. Requests for resources and reagents should be directed to and will be fulfilled by the corresponding author, RL (rong@jhu.edu). The custom Python code for quantification of spGFP fluorescence can be found within the git repository at https://github.com/RongLiLab/Wang-et-al.-2022.git (*10*).

Supplementary Materials

Table S1: List of validated MAGIC regulators

Table S2: List of yeast strains and plasmids

Movie S1: 3D reconstructed SIM images showing FlucSM spGFP inside mitochondria after 90 min estradiol treatment. Mitochondrial outer membrane is labeled with Tom70-mCherry.

Movie S2: 3D reconstructed SIM images showing FUS^{P525L} spGFP inside mitochondria after 100 min estradiol treatment. Mitochondrial outer membrane is labeled with Tom70-mCherry.

Figure 1

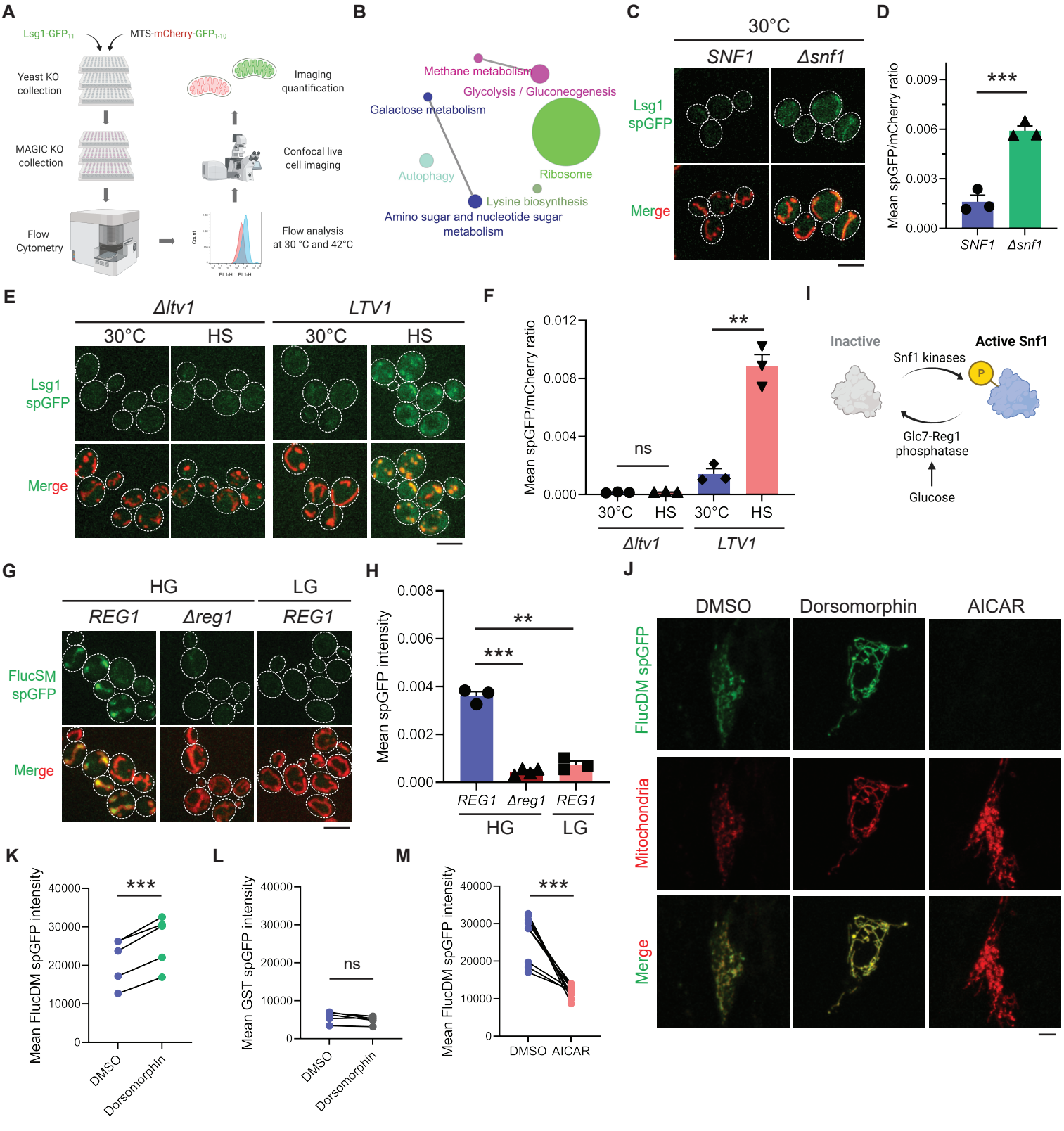
A
Lsg1-GFP11
MTS-mCherry-GFP1-10
Yeast KO collection
MAGIC KO collection
Flow Cytometry
Imaging quantification
Confocal live cell imaging
Flow analysis at 30 °C and 42°C
B
Methane metabolism
Glycolysis / Gluconeogenesis
Galactose metabolism
Autophagy
Ribosome
Lysine biosynthesis
Amino sugar and nucleotide sugar metabolism
C
30°C
SNF1
Δsnf1
Lsg1 spGFP
Merge
D
Mean spGFP/mCherry ratio
***
SNF1
Δsnf1
E
Δltv1
LTV1
30°C
HS
Lsg1 spGFP
Merge
F
Mean spGFP/mCherry ratio
**
ns
30°C
HS
Δltv1
LTV1
I
Inactive
Active Snf1
Snf1 kinases
P
Glc7-Reg1 phosphatase
Glucose
G
HG
LG
REG1
Δreg1
FlucSM spGFP
Merge
H
Mean spGFP intensity
**
***
REG1
Δreg1
HG
LG
J
DMSO
Dorsomorphin
AICAR
FlucDM spGFP
Mitochondria
Merge
K
Mean FlucDM spGFP intensity
***
DMSO
Dorsomorphin
L
Mean GST spGFP intensity
ns
DMSO
Dorsomorphin
M
Mean FlucDM spGFP intensity
***
DMSO
AICAR

Figure 1. MAGIC regulators revealed by a genome-wide screen in yeast and validations in human RPE-1 cells. (**A**) Workflow of the spGFP-based genetic screen in yeast. (**B**) KEGG pathway analysis of validated mutants that affect MAGIC. The size of the node indicates the number of genes identified. Pathways with at least two associated genes are shown. (**C**, **D**) Representative images (C) and quantification (D) of Lsg1 spGFP signal in WT and *Δsnf1* cells at 30 °C. Shown in (C): Top, Lsg1 spGFP; Bottom, merged images of spGFP and mitochondria labeled with MTS-mCherry. Shown in (D): means ± SEM of spGFP/mCherry ratio. Unpaired two-tailed *t*-test. (**E**, **F**) Representative images (E) and quantification (F) of Lsg1 spGFP signal in *Δltv1* and wild-type *LTV1* cells at 30 °C and after HS. Shown in (F): means ± SEM of spGFP/mCherry ratio. Paired two-tailed *t*-test. HS: heat shock. (**G**, **H**) Representative images (G) and quantification (H) of FlucSM spGFP signals in WT (*REG1*) cells in HG or LG, and *Δreg1* cells in HG. Shown in (G): Top, FlucSM spGFP; Bottom, merged images of spGFP and mitochondria labeled with Tom70-mCherry. Shown in (H): means ± SEM of spGFP intensity. Paired (*REG1* in HG vs. LG) or unpaired (*REG1* vs. *Δreg1* in HG) two-tailed *t*-test. (**I**) Schematic diagram of Snf1 activation in yeast. (**J**) Representative images of FlucDM spGFP in RPE-1 cells treated with DMSO, dorsomorphin, or AICAR. Top, FlucDM spGFP; Middle, mitochondria-targeted mCherry; Bottom, merged images. (**K**-**M**) Flow cytometry-based quantifications of FlucDM spGFP in RPE-1 cells treated with DMSO, dorsomorphin, or AICAR (K, M), and GST spGFP in cells treated with DMSO or dorsomorphin (L). Means ± SEM of spGFP intensities are shown. Paired two-tailed *t*-test. $^{**}P < 0.01$; $^{***}P < 0.001$; ns, not significant, $P > 0.05$. HG: 2% glucose; LG: 0.1% glucose plus 3% glycerol. Scale bars, 5 μm.

Figure 1—figure supplement 1

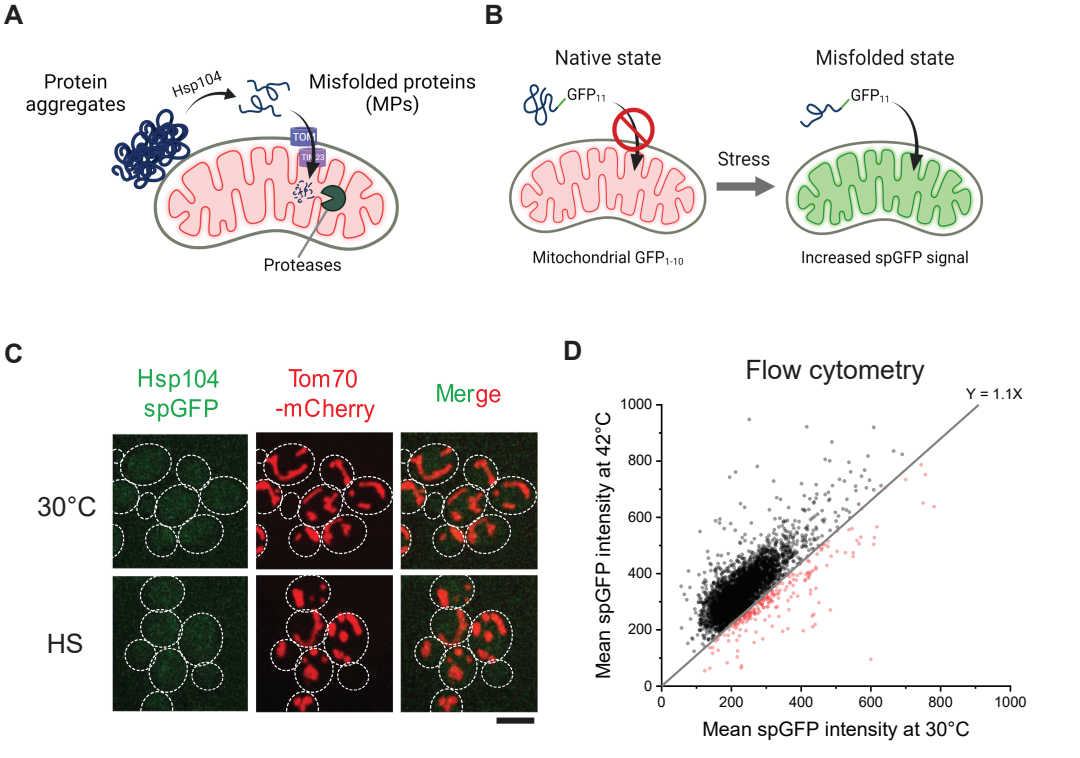

Figure 1—figure supplement 1. Schematics of MAGIC pathway and spGFP-based imaging in the whole-genome screen in yeast. (**A**) Schematic diagram of MAGIC involving the import of cytosolic misfolded proteins through mitochondrial import machineries and the subsequent degradation under proteotoxic stresses (heat shock or overload of MPs). (**B**) Schematic diagram of spGFP reporter. (**C**) Hsp104 spGFP in mitochondria at 30 °C and after heat shock (HS) at 42 °C for 30 min. Endogenous Hsp104 was tagged with GFP_{11}, while GFP_{1-10} was constitutively targeted to the mitochondrial matrix by linking to a matrix protein Grx5. Similar results were obtained by using MTS-mCherry-GFP_{1-10} (*10*). 3 biological repeats, 63 cells (30 °C) and 220 cells (HS) imaged. Scale bar, 5 μm. (**D**) Flow cytometry readouts of yeast knockout mutants at 30 °C and after 42 °C HS. Red dots represent mutants that failed to show an increase in Lsg1 spGFP after HS.

Figure 1—figure supplement 2

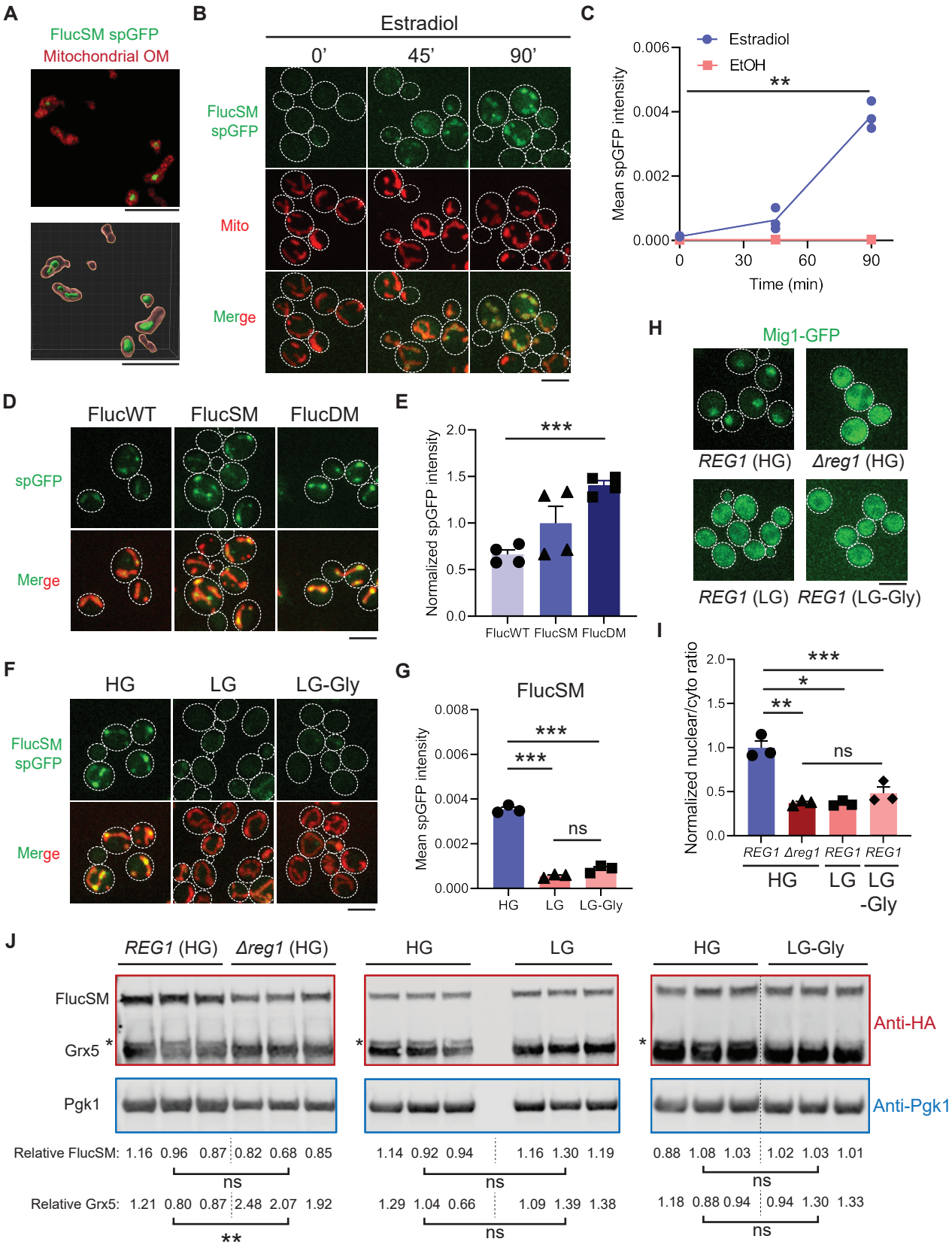

Figure 1—figure supplement 2. Snf1 regulates the accumulation of misfolded proteins in mitochondria after acute overexpression of FlucSM. (**A**) Representative super-resolution imaging for FlucSM spGFP signal in mitochondria after 90 min estradiol induction. Top, maximum projection. Bottom, 3D rendering. OM: outer membrane labeled by Tom70-mCherry. (**B**, **C**) Representative images (B) and quantification (C) of time-dependent accumulation of FlucSM spGFP signal in mitochondria at 30 °C after estradiol or ethanol treatment in HG medium. Shown in (B): Top, FlucSM spGFP; Middle: mitochondria labeled with Tom70-mCherry; Bottom: merged images. Shown in (C): means ± SEM of spGFP intensity. Paired two-tailed *t*-test comparing 0 min and 90 min estradiol treatment. (**D**, **E**) Representative images (D) and quantification (E) of FlucWT, FlucSM, and FlucDM spGFP after 90 min estradiol treatment in HG medium. Shown in (E): means ± SEM of normalized spGFP intensities. Unpaired two-tailed *t*-test between FlucWT and FlucDM. (**F**, **G**) Representative images (F) and quantification (G) of FlucSM spGFP in cells that grew in HG, LG, and LG-Gly media. Shown in (G): means ± SEM of spGFP intensity. Paired two-tailed *t*-test. (**H**, **I**) Representative images (H) and quantification (I) of the nuclear-cytoplasmic translocation of Mig1-GFP. Shown in (I): means ± SEM of normalized Mig-GFP nuclear-cytoplasmic ratio. Paired (WT in HG vs. LG or LG-Gly) or unpaired (WT vs. *Δreg1* in HG) two-tailed *t*-test, and one-way ANOVA for comparing *Δreg1* in HG, WT in LG, and WT in LG-Gly). (**J**) Immunoblots of FlucSM-HA-GFP_{11} and Grx5-HA-$GFP_{1\text{-}10}$ in cell lysates. Relative FlucSM levels (FlucSM/Pgk1) and relative Grx5 levels (matured Grx5/Pgk1) of three biological repeats are shown. Paired (HG vs. LG or LG-Gly) or unpaired (WT vs. *Δreg1* in HG) two-tailed *t*-test. Asterisks indicate the precursor species of Grx5-HA-$GFP_{1\text{-}10}$ that are excluded from quantification. HG: 2% glucose; LG: 0.1% glucose plus 3% glycerol; LG-Gly: 0.1% glucose. EtOH: ethanol. *$P < 0.05$; **$P < 0.01$; ***$P < 0.001$; ns, not significant, $P > 0.05$. Scale bars, 5 μm.

Figure 1—figure supplement 3

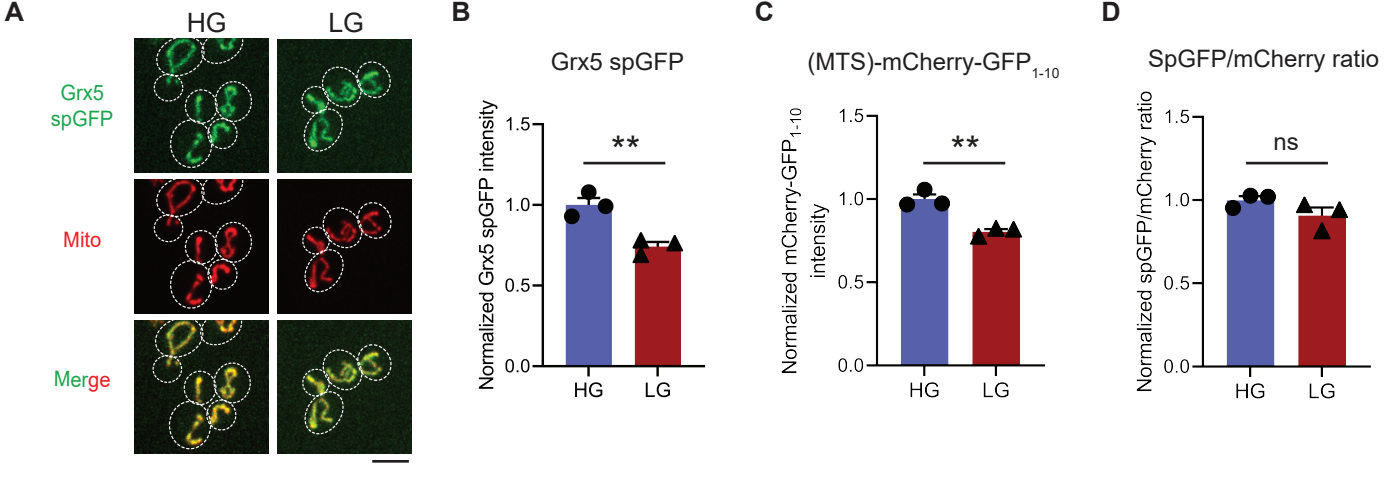

Figure 1—figure supplement 3. **Snf1 activation only modestly affects spGFP reconstitution.** (**A-D**) Representative images (A) and quantification of Grx5 spGFP (B), MTS-mCherry-GFP1-10 (C) and spGFP-to-mCherry ratio (D) in HG or LG medium. Means ± SEM are shown in (B-D). Unpaired two-tailed *t*-test. ***P* < 0.01; ns, not significant, *P* > 0.05. HG: 2% glucose; LG: 0.1% glucose plus 3% glycerol. Scale bars, 5 μm.

Figure 2

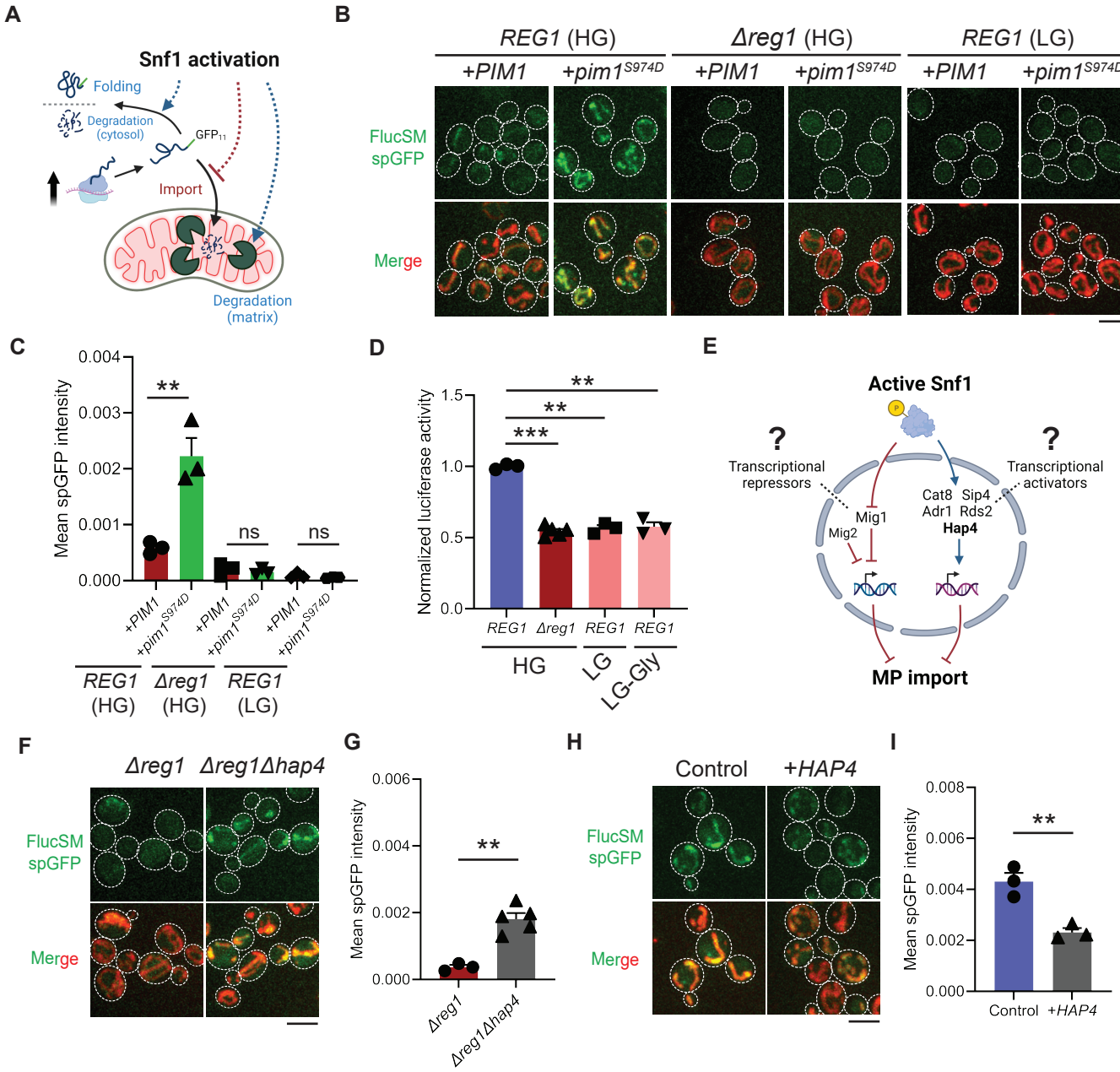
A
Snf1 activation
Folding
Degradation (cytosol)
GFP11
Import
Degradation (matrix)
B
REG1 (HG)
Δreg1 (HG)
REG1 (LG)
+PIM1
+pim1S974D
FlucSM spGFP
Merge
C
Mean spGFP intensity
0.004
0.003
0.002
0.001
0.000
**
ns
ns
+PIM1
+pim1S974D
REG1 (HG)
Δreg1 (HG)
REG1 (LG)
D
Normalized luciferase activity
1.5
1.0
0.5
0.0
**
**
***
REG1
Δreg1
REG1
REG1
HG
LG
LG-Gly
E
Active Snf1
?
Transcriptional repressors
Mig1
Mig2
?
Transcriptional activators
Cat8 Sip4
Adr1 Rds2
Hap4
MP import
F
Δreg1
Δreg1Δhap4
FlucSM spGFP
Merge
G
Mean spGFP intensity
0.006
0.004
0.002
0.000
**
Δreg1
Δreg1Δhap4
H
Control
+HAP4
FlucSM spGFP
Merge
I
Mean spGFP intensity
0.008
0.006
0.004
0.002
0.000
**
Control
+HAP4

Figure 2. Snf1 negatively regulates mitochondrial import of cytosolic misfolded proteins. (**A**) Schematic diagram showing three possible explanations for reduced spGFP in mitochondria of Snf1-active cells: reduced MPs, blocked import, or enhanced degradation. (**B**, **C**) Representative images (B) and quantification (C) of FlucSM spGFP in Snf1-inactive and Snf1-active cells overexpressing copper-inducible *PIM1* or $pim1^{S974D}$. Shown in (C): means ± SEM of spGFP intensities. Unpaired two-tailed *t*-test. (**D**) Relative *in vivo* luciferase activity after 90 min of estradiol treatment. Means ± SEM of normalized FlucSM activity are shown. Paired (WT in different media) or unpaired (WT vs. *Δreg1* in HG) two-tailed *t*-test. LG-Gly: 0.1% glucose only. (**E**) Hypothetical regulations of import of MPs through transcriptional repressors and activators downstream of Snf1 activation. (**F**, **G**) Representative images (F) and quantification (G) of FlucSM spGFP in *Δreg1* and *Δreg1Δhap4* cells in HG medium. Shown in (G): means ± SEM of spGFP intensity. Unpaired two-tailed *t*-test. (**H**, **I**) Representative images (H) and quantification (I) of FlucSM spGFP in wild-type cells (control) or with constitutive overexpression of *HAP4* in HG medium. Shown in (I): means ± SEM of spGFP intensities. Unpaired two-tailed *t*-test. $^{**}P < 0.01$; $^{***}P < 0.001$; ns, not significant, $P > 0.05$. Scale bars, 5 μm.

Figure 2—figure supplement 1

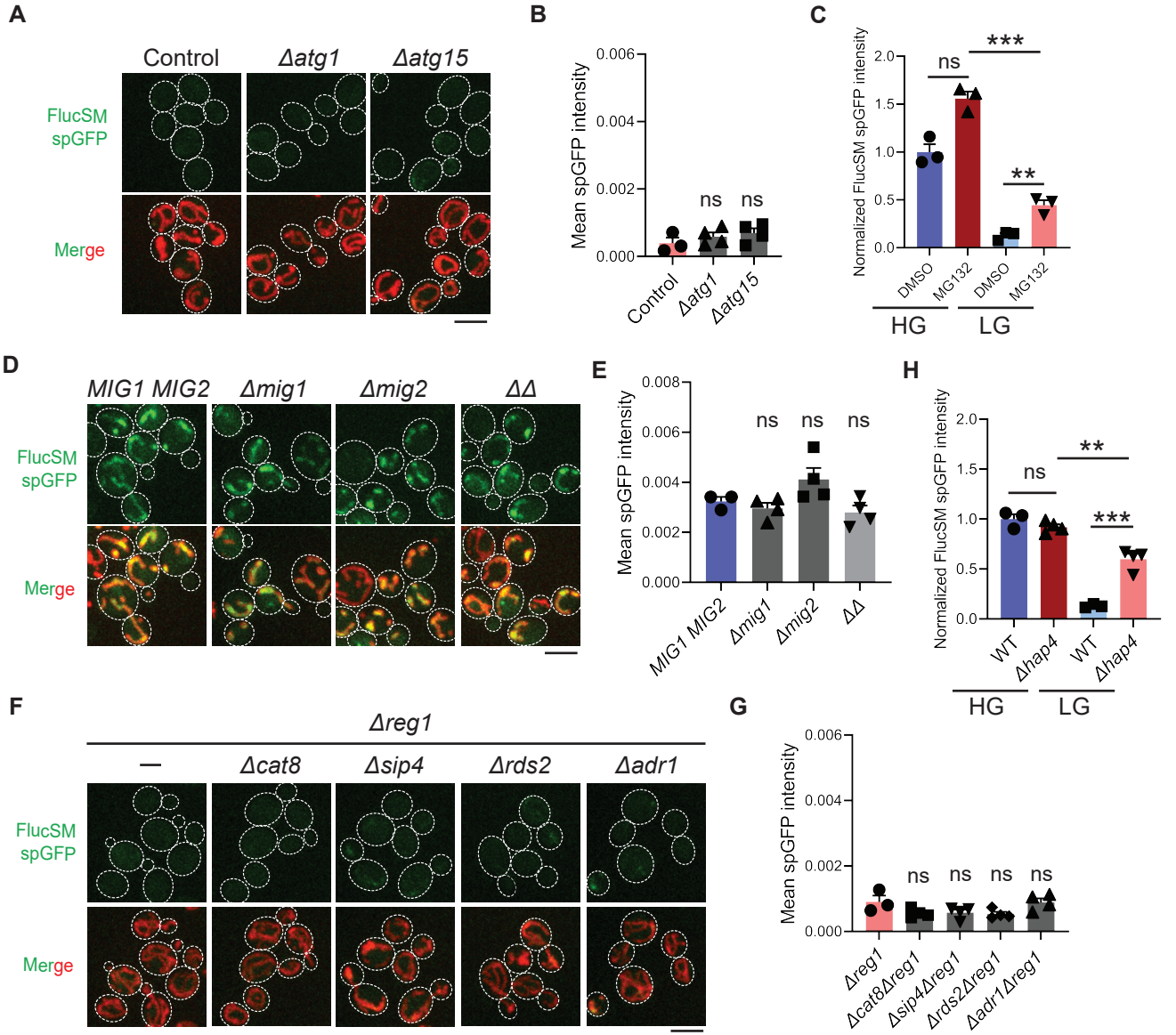

Figure 2—figure supplement 1. Reduced accumulation of misfolded proteins in mitochondria under Snf1 activation is neither caused by elevated autophagy nor mediated by certain transcription factors. (**A**, **B**) Representative images (A) and quantification (B) of FlucSM spGFP in control cells and autophagy-deficient mutants in LG medium. Shown in (A): means ± SEM of spGFP intensity. Unpaired two-tailed *t*-test between control and each mutant. (**C**) Quantification of FlucSM spGFP signals in *Δpdr5* cells treated with DMSO or 80 μM MG132 for 90 min during estradiol induction. Means ± SEM of normalized spGFP intensities are shown. Paired two-tailed *t*-test. (**D**, **E**) Representative images (D) and quantification (E) of FlucSM spGFP in wild-type (*MIG1 MIG2*), *Δmig1*, *Δmig2*, and *Δmig1Δmig2* (*ΔΔ*) cells in HG medium. Shown in (E): means ± SEM of spGFP intensity. Unpaired two-tailed *t*-test between WT and each mutant. (**F**, **G**) Representative images (F) and quantification (G) of FlucSM spGFP in *Δreg1* and double mutant cells in HG medium. Shown in (G): means ± SEM of spGFP intensity. Unpaired two-tailed *t*-test between *Δreg1* and each double mutant. (**H**) Quantification of FlucSM spGFP signals in WT or *Δhap4* cells. Unpaired two-tailed *t*-test between WT and *Δhap4*. Pair two-tailed *t*-test for *Δhap4* cells in different medium. $^{**}P < 0.01$; $^{***}P < 0.001$; ns, not significant, $P > 0.05$. Scale bars, 5 μm.

Figure 3

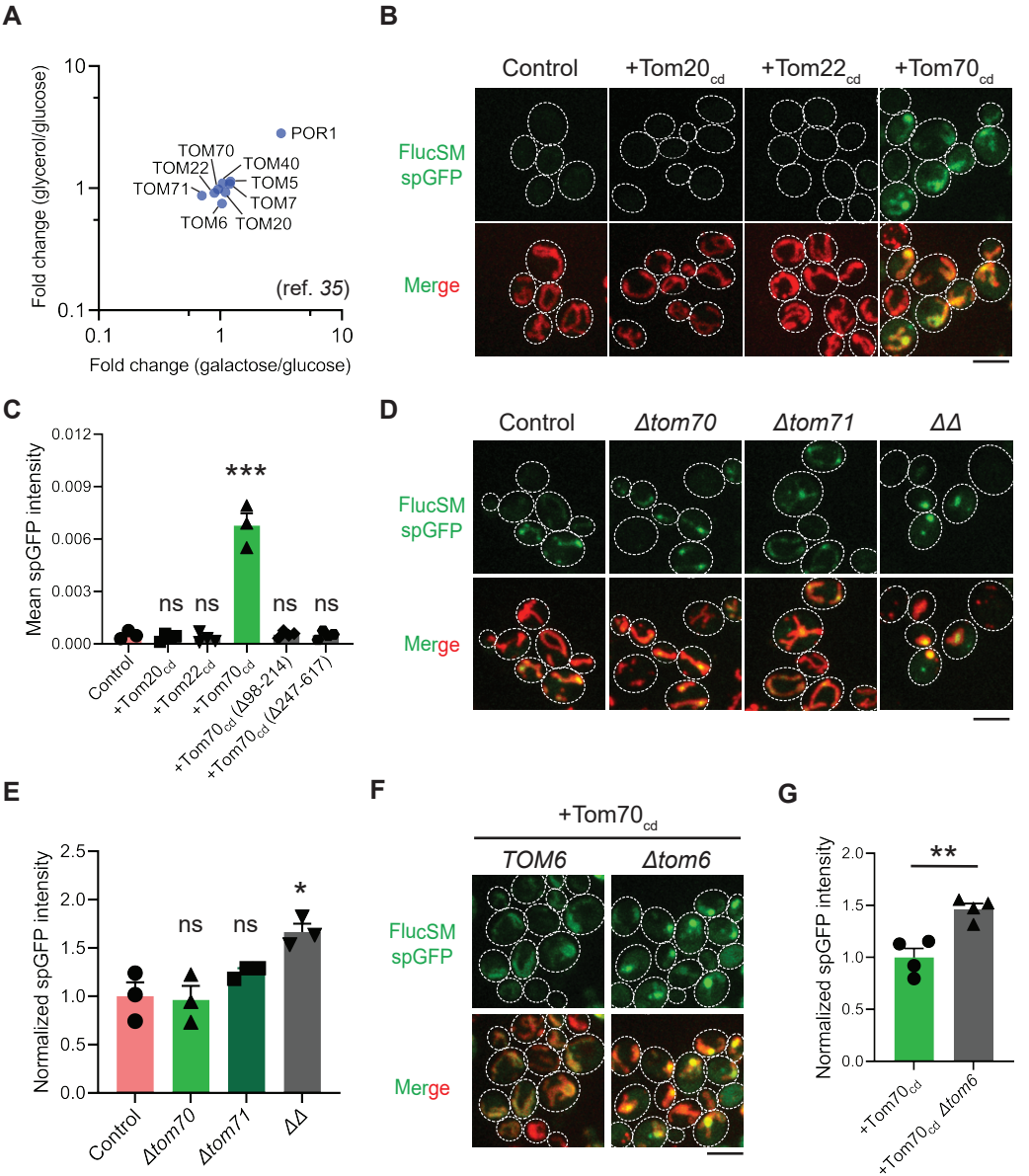
A
Fold change (glycerol/glucose)
Fold change (galactose/glucose)
10
1
0.1
0.1
1
10
POR1
TOM70
TOM22
TOM71
TOM40
TOM5
TOM7
TOM6
TOM20
(ref. 35)
B
Control
+Tom20cd
+Tom22cd
+Tom70cd
FlucSM spGFP
Merge
C
Mean spGFP intensity
0.012
0.009
0.006
0.003
0.000
***
ns
ns
ns
ns
Control
+Tom20cd
+Tom22cd
+Tom70cd
+Tom70cd (Δ98-214)
+Tom70cd (Δ247-617)
D
Control
Δtom70
Δtom71
ΔΔ
FlucSM spGFP
Merge
E
Normalized spGFP intensity
2.5
2.0
1.5
1.0
0.5
0.0
ns
ns
*
Control
Δtom70
Δtom71
ΔΔ
F
+Tom70cd
TOM6
Δtom6
FlucSM spGFP
Merge
G
Normalized spGFP intensity
2.0
1.5
1.0
0.5
0.0
**
+Tom70cd
+Tom70cd Δtom6

Figure 3. Mechanisms underlying Snf1-regulated MP import into mitochondria. (**A**) Fold changes in protein abundance of TOM complex components in glucose-limiting condition (glycerol or galactose) compared to glucose-rich condition. Raw data are retrieved from a published quantitative mass spectrometry dataset (*35*). (**B**, **C**) Representative images (B) and quantification (C) of FlucSM spGFP in wild-type control cells and cells overexpressing $Tom20_{cd}$, $Tom22_{cd}$, and $Tom70_{cd}$ (C), or truncated $Tom70_{cd}$ variants (Figure 3—figure supplement 1D) in LG medium. Shown in (C): means ± SEM of spGFP intensities. Unpaired two-tailed *t*-test between control and overexpression strains. (**D**, **E**) Representative images (D) and quantification (E) of FlucSM spGFP in wild-type control, *Δtom70*, *Δtom71*, and *Δtom70 Δtom71* (*ΔΔ*) cells in HG medium. Shown in (D): Top, FlucSM spGFP; Bottom, merged images of spGFP and mitochondria labeled with mCherry-Fis1TM. Shown in (E): means ± SEM of normalized spGFP intensity. Unpaired two-tailed *t*-test. (**F**, **G**) Representative images (F) and quantification (G) of FlucSM spGFP in control and *Δtom6* cells overexpressing $Tom70_{cd}$ in LG medium. Shown in (G): means ± SEM of normalized spGFP intensities. Unpaired two-tailed *t*-test. *$P < 0.05$; **$P < 0.01$; ***$P < 0.001$; ns, not significant, $P > 0.05$. Scale bars, 5 μm.

Figure 3—figure supplement 1

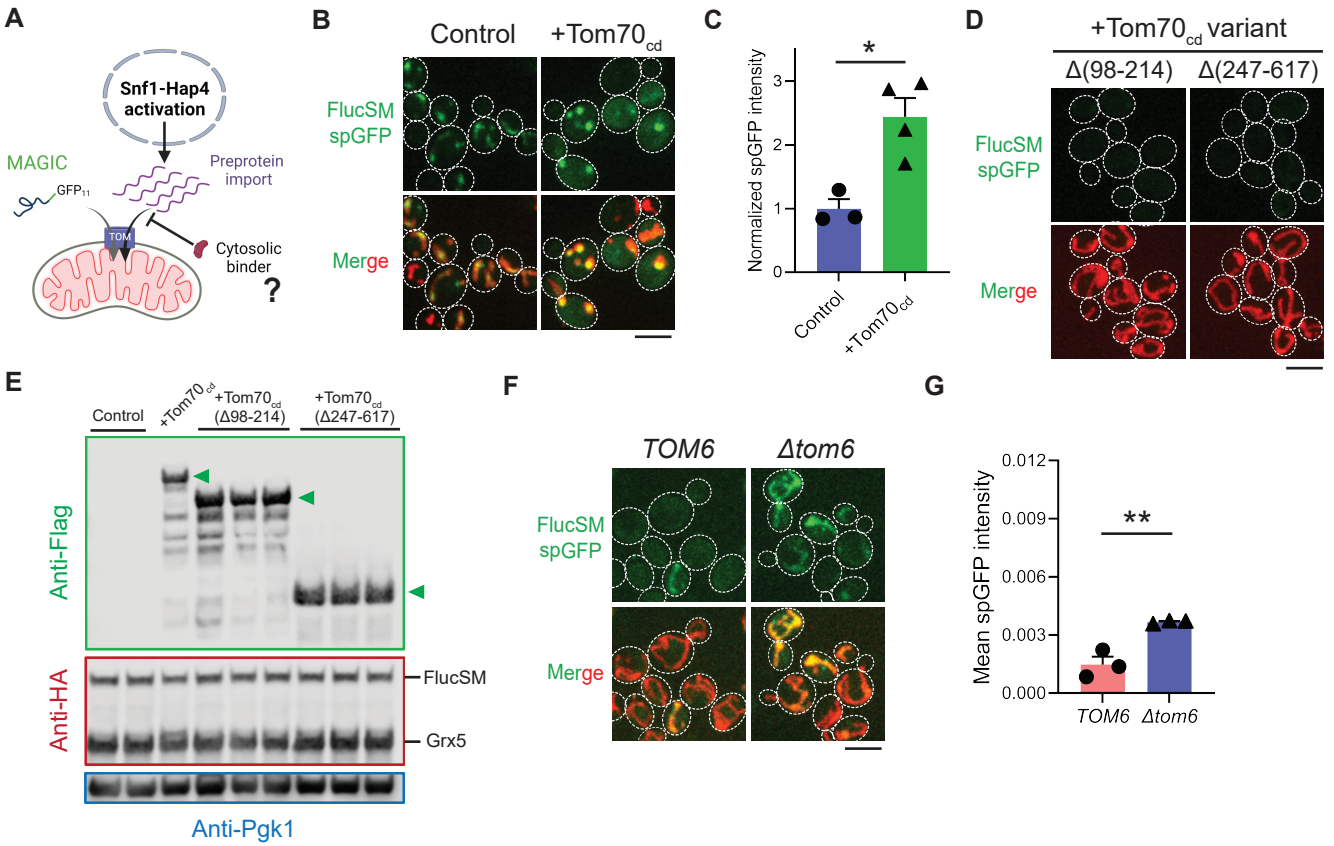

Figure 3—figure supplement 1. Role of Tom70 cytosolic domain and Tom6 in regulating misfolded protein import. (**A**) Working model of preprotein import and misfolded protein import through limited TOM channels. Introducing cytosolic binders of preproteins may release the import capacity for misfolded proteins. (**B**, **C**) Representative images (B) and quantification (C) of FlucSM spGFP in cells with or without $Tom70_{cd}$ overexpression in HG medium. Shown in (C): means ± SEM of normalized spGFP intensity. Unpaired two-tailed *t*-test. (**D**) Representative images of FlucSM spGFP in cells overexpressing truncated Tom70cd variants in LG medium. Quantification is shown in Figure 4C. (**E**) Immunoblots of overexpressed $Tom70_{cd}$-3×Flag variants in lysates of cells that grew in LG medium. Anti-HA panel shows FlucSM-HA-GFP_{11} after 90min estradiol treatment and constitutively expressed Grx5-HA-GFP_{1-10}. Arrowheads indicate intact $Tom70_{cd}$-3×Flag variants. (**F**, **G**) Representative images (F) and quantification (G) of FlucSM spGFP in WT and *Δtom6* cells in LG medium. Shown in (G): means ± SEM of spGFP intensities. Unpaired two-tailed *t*-test. **P* < 0.05; ***P* < 0.01; ns, not significant, *P* > 0.05. Scale bars, 5 μm.

Figure 4

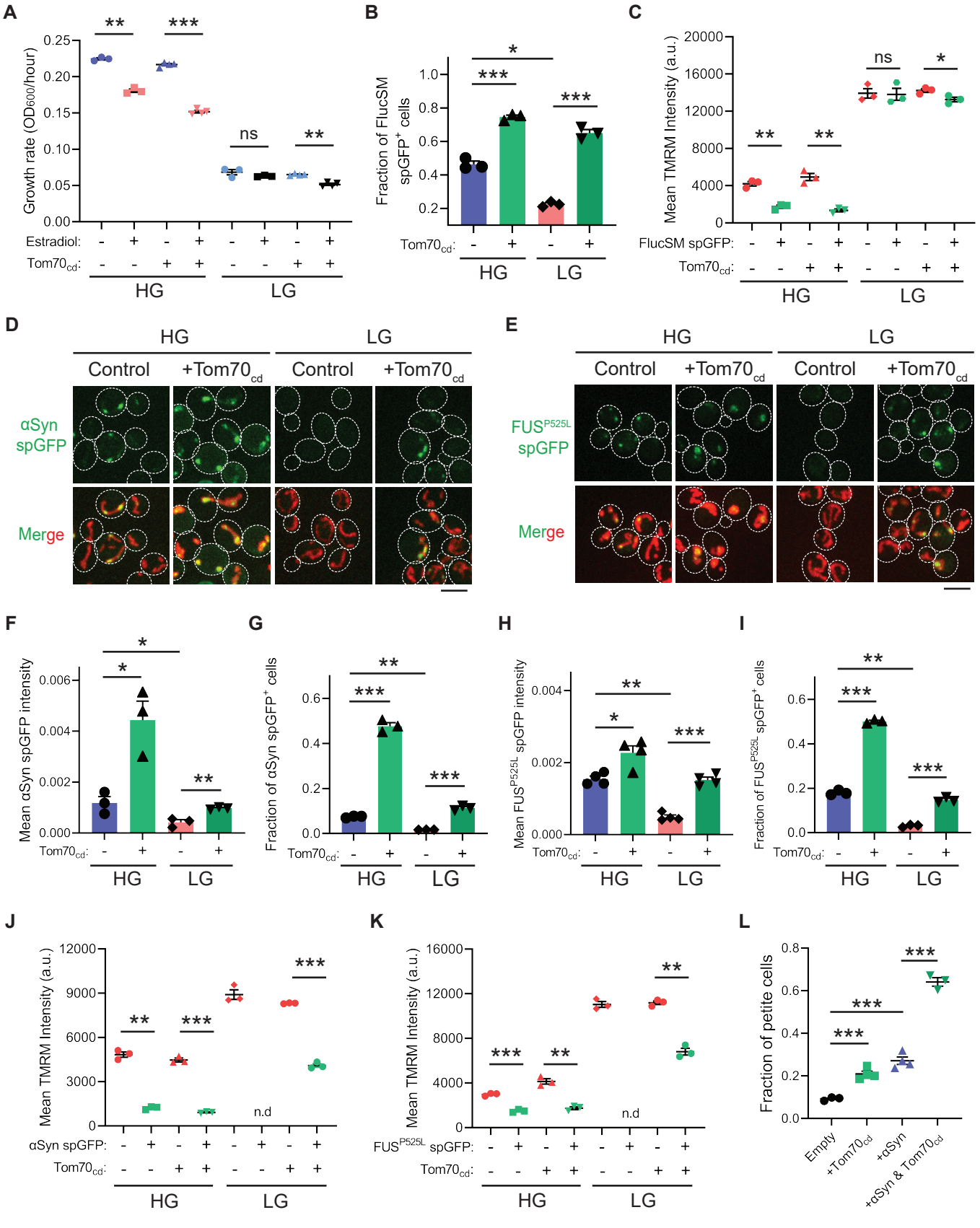
A
Growth rate (OD600/hour)
Estradiol:
Tom70cd:
HG
LG
B
Fraction of FlucSM spGFP+ cells
Tom70cd:
HG
LG
C
Mean TMRM Intensity (a.u.)
FlucSM spGFP:
Tom70cd:
HG
LG
D
HG
LG
Control
+Tom70cd
αSyn spGFP
Merge
E
HG
LG
Control
+Tom70cd
FUSP525L spGFP
Merge
F
Mean αSyn spGFP intensity
Tom70cd:
HG
LG
G
Fraction of αSyn spGFP+ cells
Tom70cd:
HG
LG
H
Mean FUSP525L spGFP intensity
Tom70cd:
HG
LG
I
Fraction of FUSP525L spGFP+ cells
Tom70cd:
HG
LG
J
Mean TMRM Intensity (a.u.)
n.d
αSyn spGFP:
Tom70cd:
HG
LG
K
Mean TMRM Intensity (a.u.)
n.d
FUSP525L spGFP:
Tom70cd:
HG
LG
L
Fraction of petite cells
Empty
+Tom70cd
+αSyn
+αSyn & Tom70cd

Figure 4. Snf1 activation protects cellular fitness against proteotoxic stress. (**A**) Growth rates of wild-type cells and cells overexpressing $Tom70_{cd}$ with (Estradiol) or without (EtOH) FlucSM expression in HG and LG medium. Means ± SEM of OD_{600} or growth rates are shown. Paired two-tailed *t*-test. (**B**) Fraction of FlucSM spGFP-positive cells measured by flow cytometry. Means ± SEM are shown. Unpaired two-tailed *t*-test for cells growing in the same medium. Paired two-tailed *t*-test for control cells growing in different medium. (**C**) Comparisons of mitochondrial membrane potential between FlucSM spGFP-negative and spGFP-positive cells measured by TMRM. Means ± SEM are shown. Paired two-tailed *t*-test. (**D**-**I**) Representative images and quantifications of α-synuclein (αSyn) spGFP and FUS^{P525L} spGFP signal. Shown in (F, H): means ± SEM of spGFP intensity measured by confocal imaging. Shown in (G, I): means ± SEM of fraction of spGFP-positive cells measured by flow cytometry. Unpaired two-tailed *t*-test for cells growing in the same medium. Paired two-tailed *t*-test for control cells between HG and LG medium. (**J**, **K**) Comparisons of membrane potential between αSyn or FUS^{P525L} spGFP-negative and spGFP-positive cells measured by TMRM. Means ± SEM are shown. Paired two-tailed *t*-test. n.d.: not determined due to limited positive cell counts in control cells growing in LG medium. (**L**) Fraction of respiratory-deficient petite cells measured by using tetrazolium overlay. Means ± SEM are shown. Unpaired two-tailed *t*-test. HG: 2% glucose; LG: 0.1% glucose plus 3% glycerol. *$P < 0.05$; **$P < 0.01$; ***$P < 0.001$; ns, not significant, $P > 0.05$. Scale bars, 5 μm.

Figure 4—figure supplement 1

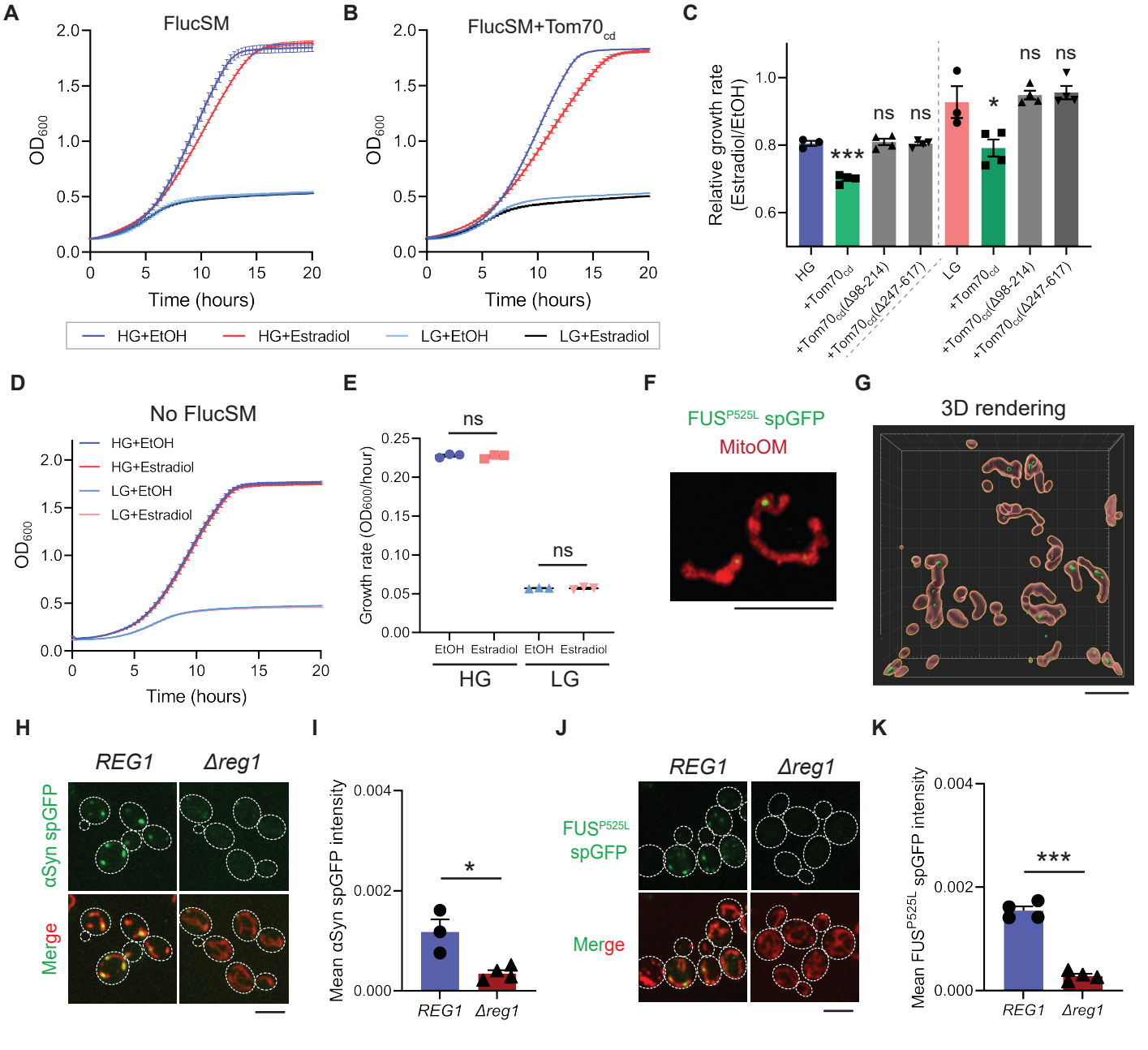

Figure 4—figure supplement 1. Snf1 activation protects against stress associated with FlucSM overexpression and prevents the accumulation of α-synuclein and FUS^{P525L} in yeast mitochondria. (**A**, **B**) Growth curves of wild-type control cells (A) and cells overexpressing Tom70$_{cd}$ (B) with (Estradiol) or without (EtOH) FlucSM expression in HG and LG medium. Fitted growth rates are shown in Figure 4A. (**C**) Relative growth rates of control cells and cells overexpressing Tom70$_{cd}$ variants. Means ± SEM are shown. Unpaired two-tailed *t*-test between control and Tom70$_{cd}$ variants that grew in the same medium (HG or LG). (**D**, **E**) Growth curves (D) and growth rates (E) of BY4741 cells lack of FlucSM spGFP reporter in HG and LG medium. Means ± SEM are shown. Paired two-tailed *t*-test. (**F**, **G**) Representative super-resolution imaging for FUS^{P525L} spGFP signal in mitochondria after 100 min of estradiol induction. Shown in (F): maximum projection image. Shown in (G): 3D rendered image. Mitochondrial OM: Mitochondrial outer membrane labeled with Tom70-mCherry. (**H-K**) Representative images (H, J) and quantification (I, K) of α-synuclein (αSyn) spGFP signal FUS^{P525L} spGFP signal in wild-type (*REG1*) and *Δreg1* cells. Shown in (I, K): means ± SEM of spGFP intensity. Unpaired two-tailed *t*-test. HG: 2% glucose; LG: 0.1% glucose plus 3% glycerol. EtOH: ethanol. *$P < 0.05$; **$P < 0.01$; ns, not significant, $P > 0.05$. Scale bars, 5 μm.

Figure 5

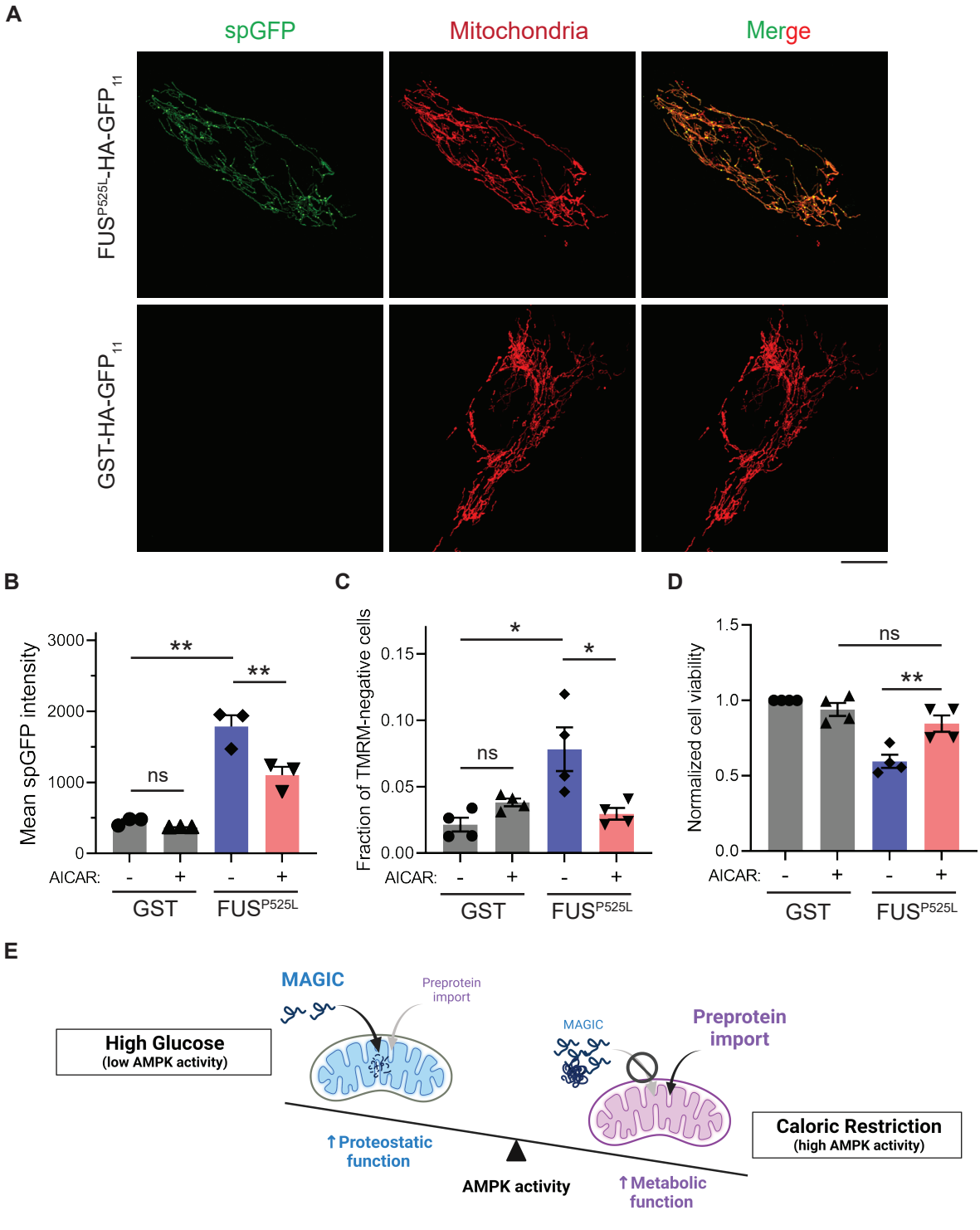
A
spGFP
Mitochondria
Merge
FUSP525L-HA-GFP11
GST-HA-GFP11
B
Mean spGFP intensity
3000
2000
1000
0
**
**
ns
AICAR:
-
+
-
+
GST
FUSP525L
C
Fraction of TMRM-negative cells
0.15
0.10
0.05
0.00
*
*
ns
AICAR:
-
+
-
+
GST
FUSP525L
D
Normalized cell viability
1.5
1.0
0.5
0.0
ns
**
AICAR:
-
+
-
+
GST
FUSP525L
E
MAGIC
Preprotein import
High Glucose
(low AMPK activity)
MAGIC
Preprotein import
Caloric Restriction
(high AMPK activity)
↑ Proteostatic function
AMPK activity
↑ Metabolic function

Figure 5. AMPK activation prevents the accumulation of ALS-associated FUS^{P525L} in mitochondria of RPE-1 cells and alleviates FUS-induced cytotoxicity. (**A**, **B**) Representative images (A) and flow cytometry quantification (B) of FUS^{P525L} spGFP and GST spGFP in mitochondria of RPE-1 cells treated with or without AICAR. Shown in (B): Means ± SEM of spGFP intensity. (**C**, **D**) Fraction of TMRM-negative cells (C) and normalized cell viability (D) of RPE-1 cells expressing GST-HA-GFP$_{11}$ or FUS^{P525L}-HA-GFP$_{11}$ with or without AICAR treatment. Means ± SEM are shown. (**E**)Working model wherein Snf1/AMPK balances the metabolic and proteostasis function of mitochondria in response to glucose availability. Paired two-tailed *t*-test for the same cell line treated with drug or control medium. Unpaired two-tailed *t*-test between cell lines expressing GST and FUS^{P525L}. *$P < 0.05$; **$P < 0.01$; ns, not significant, $P > 0.05$. Scale bars, 10 μm.

Materials and Methods

Yeast strains, plasmids and culture media

Yeast strains used in this study are based on the BY4741 strain background and listed in Table S2. Gene deletion and protein tagging were performed through PCR-mediated homologous recombination (*65*) and verified by PCR genotyping. MAGIC YKO collection was constructed by incorporating MTS-mCherry-GFP_{1-10} under GPD promoter into the TRP1 locus and tagging endogenous Lsg1 with GFP_{11} in the YKO collection (*18*). *Δreg1* and YKO strains harboring the deletion of the transcriptional factor downstream of Snf1 were freshly made and validated for at least three independent colonies.

Human α-synuclein tagged with GFP11 under GPD promoter was cloned and inserted into the *ura3Δ0* locus. FlucSM-HA-GFP_{11} and FUS^{P525L}-HA-GFP_{11} under GAL1 promoter were cloned from plasmids from our previous study (*10*) and plasmid 416Gal-FUS-P525L-YFP, a gift from Aaron Gitler (Addgene plasmid #29628). FlucWT-HA-GFP_{11} and FlucDM-HA-GFP_{11} plasmids were constructed using site-directed mutagenesis kit (NEB) based on FlucSM-HA-GFP_{11}. Both GFP_{11}-tagged Fluc proteins and GEM transcriptional factor (cloned from pJW1663, Addgene plasmid #112037) were stably integrated into yeast genome. $GFP_{1–10}$ was fused with the mitochondrial matrix protein Grx5 under GPD promoter, except in experiments involving *PIM1* or $pim1^{S974D}$ mutant and α-synuclein spGFP where $GFP_{1–10}$ was fused to the C-terminus of endogenous Grx5 to avoid signal saturation. Wild-type *PIM1* or $pim1^{S974D}$ mutant under CUP1 promoter, *HAP4*, cytosolic domain of Tom20 (1-97 aa), Tom22 (38-617aa), Tom70 (38-617aa) and truncated variants of Tom70cd under GPD promoter were cloned and stably integrated into yeast genome. Mitochondrial outer membrane was labeled with Tom70-mCherry or Tom70-RFP, except for the Tom70/71 deletion experiments in which mitochondria were labeled with mCherry-Fis1TM (*8*).

MAGIC YKO library construction, flow cytometry, and imaging during high-throughput screen were performed with synthetic defined minus histidine (SD-His) medium. Synthetic complete (SC) supplemented with 2% glucose (HG), 0.1% glucose plus 3% glycerol (LG), or 0.1% glucose (LG-Gly) was used for confocal imaging, luciferase assays, biochemistry, and TMRM staining. YEP medium (yeast extract-peptone) supplemented with 2% glucose (HG) or 0.1% glucose plus 3% glycerol (LG) was used for growth assays. Optical density at 600 nm (OD_{600}) was used to estimate the amount of yeast cells used in the various experiments.

Drug treatments

β–estradiol (E2758, MilliporeSigma) was dissolved in H_2O and added at a final concentration of 1 μM. $CuSO_4$ (C1297, MilliporeSigma) was dissolved in H_2O and added at a final concentration of 0.5 mM. D-luciferin potassium salt (LUCK, GoldBio) was freshly dissolved in appropriate yeast media at a final concentration of 0.5 mM. Dorsomorphin (S7840, Selleck Chemicals; 11967, Cayman Chemical) dissolved in DMSO was added to RPE-1 cells at the final concentration of 10 μM for 24 hours (*66*). AICAR was dissolved in DMSO (S1802, Selleck Chemicals) and added at the final concentration of 2 mM for 48 hours in the FlucDM experiment, or dissolved directly in media at the concentration of 2 mM (10010241, Cayman Chemical) for the FUS^{P525L} experiment (*67*). MG132 (C2211, MilliporeSigma) was dissolved in DMSO and added to YEP-based medium at a final concentration of 80 μM.

Yeast library construction and genome-wide screen

MAGIC YKO was constructed with a two-step transformation using the Frozen-EZ Yeast Transformation II Kit (T2001, Zymo Research) following the microscale protocol in 96-well format. First, knockout strains were grown to saturation in deep-well plates containing 1 ml of YPD broth with G418 (200 µg/mL, Corning). 150 µL of refreshed mid-log phase cultures and 0.2 µg of MTS-mCherry-GFP$_{1-10}$-clonNat DNA were used in the transformation setup on the epMotion 5075 liquid handling workstation (Eppendorf). To optimize transformation efficiency, the transformation mixtures were incubated for 2 hours and at the end of transformation they were transferred into deep-well plates with 4 volumes of YPD for 2 hours of outgrowth at 30 °C. The transformants were selected for 4-5 days in 1 ml of YPD broth with clonNAT (200 µg/mL, GoldBio), resulting in the intermediate MTS-mCherry-GFP$_{1-10}$-clonNat library. Then the Lsg1-HA-GFP$_{11}$ tagging PCR product was integrated into the genome of the intermediate strains following the same protocol, with the exception that the finial library was selected in SD-His medium.

Total 4645 YKO strains with Lsg1 spGFP reporter were cultured in 96-well plates, and spGFP intensities before and after heat shock (30 min at 42 °C) were measured at 488 nm excitation with appropriate filters on Attune NxT flow cytometer equipped with an auto sampler (Thermo). After subtracting background from the populational mean spGFP intensity, KOs displaying different spGFP pattern were determined by a cutoff (smaller than 1.1-fold increase after heat shock) and further validated by live cell confocal imaging. Based on the phenotype of mitochondrial spGFP intensity of each mutant at two imaging time points, Class 1 mutants were determined by the *P* value of comparing the spGFP/mCherry ratio of each single cell between KO and WT at permissive temperature, $P < 0.01$, and Class 2 mutants were determined by the *P* value of comparing the spGFP intensity of each single cell of before and after heat shock for the same mutant, $P > 0.01$. Genes involved in known mitochondrial import pathways were excluded from analysis.

Confocal microscopy and imaging conditions

Live cell images were acquired using a Yokogawa CSU-10 spinning disc on the side port of a Carl Zeiss 200 m inverted microscope or a Carl Zeiss LSM-780 confocal system. Laser 488 or 561 nm excitation was applied to excite GFP or mCherry, respectively, and the emission was collected through the appropriate filters onto a Hamamatsu C9100-13 EMCCD on the spinning disc confocal system or the single-photon avalanche photodiodes on the Zeiss 780 system. Regarding the multi-track acquisition, the configuration of alternating excitation was used to avoid the bleed-through of GFP (for dual color imaging, GFP or mCherry labeled controls were applied for laser and exposure settings). The spinning disc and the LSM780 were equipped with a 100×1.45 NA Plan-Apochromat objective and a 63x1.4 oil Plan-Apochromat objective, respectively. For yeast 3D imaging, 0.5 µm step size for 6 µm in total in Z; for human cells, 1 µm step size. Images were acquired using MetaMorph (version 7.0, MDS Analytical Technologies) on the CSU-10 spinning disc system and Carl Zeiss ZEN software on the LSM780.

Yeast culture condition for imaging: yeast cells were cultured in SC or SD-His with appropriate carbon source overnight at 30 °C. The cells were then refreshed in the corresponding medium for at least 3 hours at 30 °C until reaching an OD_{600} of about 0.2. For estradiol-GEM inducible systems, 1 µM of β–estradiol was added to the medium for 90 min unless indicated otherwise. For copper-inducible overexpression of *PIM1* or its mutant, 0.5 mM $CuSO_4$ was added for 2

hours, followed by the estradiol induction for 2 hours. All images in the same experiments were acquired with the same laser and exposure settings. Image processing was performed using ImageJ software (NIH) or Imaris software (Oxford Instruments Group). For visualization purposes, images were scaled with bilinear interpolation and shown as the maximum projection on Z for fluorescent channels. Cell boundaries were delineated according to white-field images.

Split-GFP quantification

Split-GFP fluorescence from confocal images was quantified by using a custom Python code described previously (*10*). In brief, mCherry and GFP intensities were summed along the z-axis, and then subjected to a random walk segmentation of the background and watershed segmentation of adjoining cells. For each cell, the mCherry channel was thresholded at 5% of maximal value to detect mitochondria, and median GFP intensity within mitochondria was calculated as spGFP intensity per cell. In the YKO imaging validation, Lsg1 spGFP/mCherry ratio of each cell was used for statistical analyses. For Lsg1 spGFP signal detected in *Δsnf1*, *Δltv1*, and *WT* cells, populational means spGFP/mCherry of at least 3 biological repeats were calculated. Adjusting Lsg1 spGFP intensity to mitochondrial mCherry intensity avoided the potential effect of changing local abundance of GFP_{1-10} on Lsg1 spGFP signal after heat shock. For estradiol-inducible systems that did not involve heat shock, populational mean spGFP intensity of each biological repeat was used for the following analyses. For the flow cytometry quantification, populational mean GFP intensities of at least 25,000 single cells were calculated for the following analyses. Most quantifications were shown as absolute intensity values with an arbitrary unit. Normalized spGFP intensities were calculated to highlight the relative changes between different strains.

Mammalian cell culture, transfection, imaging and quantification

Human RPE-1 cells were cultured in Dulbecco's Modified Eagle Medium: Nutrient Mixture F-12 (DMEM/F12) (GIBCO), supplemented with 10% (v/v) fetal bovine serum (FBS), 100 IU/ml penicillin. Transient transfections were performed with Lipofectamine 3000 (Invitrogen) according to the manufacturer's instructions. RPE-1 cells were dually transfected with MTS-mCherry-$GFP_{1–10}$ and the protein of interest tagged with GFP_{11} (2.5 μg of each plasmid was applied). For imaging, MatTek (P35G-0-14-C) dish was used to culture cells, and cells were located using the mCherry channel only. Cells were imaged or analyzed by flow cytometry after 24 or 48 hours of transfection for FUS^{P525L} or FlucDM, respectively. For flow cytometry analysis of FUS^{P525L} spGFP system, cells were permeabilized with digitonin buffer (0.32 M sucrose, 5 mM $CaCl_2$, 3 mM $Mg[Acetate]_2$, 0.1 mM EDTA, 10 mM Tris-HCl, 100 ug/ml digitonin) for 8-10 min, in order to remove spGFP signal outside of mitochondria in cytosol.

To evaluate cell death caused by FUS^{P525L} overexpression, equal number of RPE-1 cells were seeded in 6-well plates and transfected with GST or FUS^{P525L}, with or without AICAR. Compared to GST transfection control, FUS^{P525L} resulted in significant floating dead cells. Number of attached cells after 24 hours of transfection were analyzed with Attune NxT flow cytometer as a proxy for cell viability.

Cell lysates, immunoblots and antibodies

For yeast experiments, 1-2 ml of yeast cells in the indicated background and medium was collected by centrifugation and snap frozen in liquid nitrogen for storage. Pellets were disrupted, boiled in 120 μl 1X LDS sample buffer (Thermo) for 10 min, and vortexed with an equal volume

of 0.5 mm acid-washed glass beads to break cells at 4 °C for 2 min with a 1 min interval. Cell lysates were boiled for 5 min, separated from glass beads by 15,000 *g* centrifugation at room temperature for 30 sec, and analyzed by SDS-PAGE. For mammalian data, RPE-1 cells were washed with PBS and lysed with RIPA buffer (MilliporeSigma) supplemented with protease inhibitors on ice for 20-30 min. Cell lysates were further sonicated and incubated on ice for 5 min, followed by 10 min 21,200 *g* centrifugation at 4 °C. The supernatant was collected and analyzed by SDS-PAGE.

Transfer was performed using iBlot2 (Thermo) and immunoblots were developed using Clarity Western ECL substrate (Bio-Rad) for HRP-linked secondary antibodies, or directly using fluorescent IRDye secondary antibodies (LI-COR). Images were acquired by using LI-COR imaging systems and analyzed in Image Studio (LI-COR). HA-tag (C29F4) rabbit mAb #3724 from Cell Signaling Technology. PGK1 mouse mAb (22C5D8) from Invitrogen. FLAG mouse clone M2 (F1804) from MilliporeSigma. GFP Living Colors A.v. mAb clone JL-8 (632381) from Takara Bio.

Firefly luciferase assays

Firefly luciferase assays in yeast were carried out as described previously (*36*). In brief, after 90 min of estradiol induction, 100 µl of cells was vigorously mixed with 100 µl of 1 mM D-luciferin in a white 96-well plate (655073, Greiner Bio-One), and light emission was immediately measured by the luminescence detection mode in Cytation 5 (Biotek). Luciferase activities were normalized to cell density measured by OD_{600} and adjusted to total abundance of FlucSM protein measured by immunoblotting.

Mig1 nucleocytoplasmic translocation

The nucleocytoplasmic distribution of Mig1-GFP was quantified using a custom ImageJ macro and MATLAB script as described previously (*68*). In brief, nuclear protein Pus1-RFP was used to create nucleoplasmic mask for each cell (*69*). Cytoplasm was defined by a dilated nuclear mask (*68*). The nuclear-cytoplasmic ratio of each cell was calculated by dividing the mean nuclear intensity by the mean cytoplasmic intensity. Populational mean nuclear-cytoplasmic ratio of at least 3 biological replicates were used for statistical analyses.

Yeast growth curve

Yeast cells with indicated genetic background were cultured in corresponding media. Overnight cultures were refreshed for 4 hours at 30 °C and the OD_{600} of the cells was measured and adjusted to 0.05. Diluted cell suspension was added to a 96-well plate with 2 µM estradiol or ethanol as control. The wells along the perimeter of the plate were pre-filled with 200 µL cell-free medium to prevent evaporation. The OD_{600} was continuously monitored at 30 °C using Citation 5 (Biotek) every 20 min with constant shaking. Data were extracted and analyzed using the R package GroFit (https://cran.r-project.org/src/contrib/Archive/grofit/) (*70*).

Mitochondrial membrane potential measurements

Yeast cells expressing MPs and growing in appropriate medium was collected, incubated with 2.5 µM TMRM (21437, Cayman Chemical) for 15 min at 30 °C and washed twice by fresh medium before recording with Attune NxT flow cytometer equipped with appropriate filter sets. A SpGFP intensity threshold was applied so that less than 1% of cells displayed positive spGFP

in the ethanol-treated control groups with no expression of MPs. Mean TMRM intensities of at least 25,000 cells were calculated for each biological replicate.

RPE-1 cells transfected with either GST or FUS^{P525L} for 24 hours were washed once with PBS and added with complete media containing 150 nM TMRM for 30 min at 37 °C. After incubation, cells were washed with PBS and trpsonized into single cells. Cell suspensions were pelleted and re-suspended in PBS for analysis on the Attune NxT flow cytometer.

Tetrazolium overlay assay

Yeast tetrazolium overlay was performed to measure the respiratory deficiency in a yeast population as previously described (*71*). In brief, yeast cells were inoculated in YPD media at 30 °C overnight. Around 100 cells were plate on YPD plates and grew for 4 days at 30 °C. The tetrazolium test medium consists of 1.5% agar and 0.1% tetrazolium (17342, Cayman Chemical) in 0.067 M phosphate buffer at pH 7.0. Test was performed by pouring 15 ml of melted test medium at 55 °C over a YPD plate. The number of large red colonies (respiration-sufficient) and small white colonies (respiration-deficient) were counted after 1 hour of incubation at 30 °C.

Super resolution imaging

Structured illumination microscopy (SIM) images were acquired with a GE OMX-SR Super-Resolution Microscope 3D Structure Illumination (3D-SIM) equipped with high-sensitivity PCO sCMOS cameras, or LSM880-Airyscan FAST Super-Resolution microscopy equipped with 63×/1.4 PlanApo oil. GFP and mCherry were excited with 488 nm and 568 nm lasers, respectively. The SIM images were reconstructed with the Softworx and aligned following the Applied Precision protocols, and Zeiss images were reconstructed with Airyscan processing. 3D rendering was performed with Imaris (Oxford Instruments Group).

Statistical analysis

Descriptions of statistical tests and *P* values can be found in Figure Legends. At least three biological replicates were analyzed in all experiments. Statistical analyses were performed with GraphPad Prism 6.0 and Microsoft Excel. No statistical methods were used to predetermine the sample size. The experiments were not randomized, and the investigators were not blinded to allocation during experiments and outcome assessment.

Table S1: List of validated MAGIC regulators

(Highlighted in yellow: ribosome-associated genes based on KEGG)

Systematic Name	Standard Name	MAGIC Phenotype
YDR477W	SNF1	Class 1
YML016C	PPZ1	Class 1
YJR120W		Class 1
YOL055C	THI20	Class 1
YKL057C	NUP120	Class 1
YML024W	RPS17A	Class 2
YDR083W	RRP8	Class 2
YCR002C	CDC10	Class 2
YKL143W	LTV1	Class 2
YLL026W	HSP104	Class 2
YPR159W	KRE6	Class 2
YOR096W	RPS7A	Class 2
YMR116C	ASC1	Class 2
YPR057W	BRR1	Class 2
YJR074W	MOG1	Class 2
YCR068W	ATG15	Class 2
YML062C	MFT1	Class 2
YML026C	RPS18B	Class 2
YML013W	UBX2	Class 2
YMR032W	HOF1	Class 2
YNR029C	ZNG1	Class 2
YDL020C	RPN4	Class 2
YER151C	UBP3	Class 2
YMR255W	GFD1	Class 2
YMR307W	GAS1	Class 2
YOR035C	SHE4	Class 2
YOL072W	THP1	Class 2
YDL083C	RPS16B	Class 2
YOR258W	YOR258W	Class 2
YOL129W	VPS68	Class 2
YHR163W	SOL3	Class 2
YLR372W	ELO3	Class 2
YKL191W	DPH2	Class 2
YIR032C	DAL3	Class 2
YBR020W	GAL1	Class 2
YJR145C	RPS4A	Class 2
YDR085C	AFR1	Class 2
YGR019W	UGA1	Class 2
YEL068C		Class 2

YIL112W	HOS4	Class 2
YKL198C	PTK1	Class 2
YER087C-A		Class 2
YJL200C	ACO2	Class 2
YJL160C	PIR5	Class 2
YMR034C	RCH1	Class 2
YGR132C	PHB1	Class 2
YLL033W	IRC19	Class 2
YGR072W	UPF3	Class 2
YGR016W		Class 2
YCR071C	IMG2	Class 2
YER060W	FCY21	Class 2
YER075C	PTP3	Class 2
YGR129W	SYF2	Class 2
YPR146C		Class 2
YEL012W	UBC8	Class 2
YJR113C	RSM7	Class 2
YPL173W	MRPL40	Class 2
YDL057W		Class 2
YBR068C	BAP2	Class 2
YHR200W	RPN10	Class 2
YOR298C-A	MBF1	Class 2
YER056C	FCY2	Class 2
YNL081C	SWS2	Class 2
YGL114W	YGL114W	Class 2
YAR030C		Class 2
YLR053C	NRS1	Class 2
YMR089C	YTA12	Class 2
YBR058C	UBP14	Class 2
YBR175W	SWD3	Class 2
YBR231C	SWC5	Class 2
YDR073W	SNF11	Class 2
YDR115W	MRX14	Class 2
YGR136W	LSB1	Class 2
YGR159C	NSR1	Class 2
YHL033C	RPL8A	Class 2
YHR011W	DIA4	Class 2
YHR143W	DSE2	Class 2
YCL005W	LDB16	Class 2
YCL037C	SRO9	Class 2
YLR131C	ACE2	Class 2
YMR074C	SDD2	Class 2
YKL009W	MRT4	Class 2
YKL128C	PMU1	Class 2

YKL132C	RMA1	Class 2
YGR056W	RSC1	Class 2
YOR125C	CAT5	Class 2
YAL043C-a		Class 2
YLL015W	BPT1	Class 2
YOR235W	IRC13	Class 2
YJL179W	PFD1	Class 2
YLR387C	REH1	Class 2
YLR388W	RPS29A	Class 2
YDR173C	ARG82	Class 2
YGL197W	MDS3	Class 2
YGL194C	HOS2	Class 2
YGL210W	YPT32	Class 2
YPL049C	DIG1	Class 2
YGL085W	LCL3	Class 2
YNL156C	NSG2	Class 2
YKL213C	DOA1	Class 2
YKR042W	UTH1	Class 2
YKR057W	RPS21A	Class 2
YLR065C	SND2	Class 2
YIL043C	CBR1	Class 2
YIL049W	DFG10	Class 2
YIL088C	AVT7	Class 2
YIL054W		Class 2
YOL111C	MDY2	Class 2
YOL122C	SMF1	Class 2
YER091C	MET6	Class 2
YNL316C	PHA2	Class 2
YDL213C	NOP6	Class 2
YDR006C	SOK1	Class 2
YDR025W	RPS11A	Class 2
YBR297W	MAL33	Class 2
YCR025C		Class 2
YML088W	UFO1	Class 2
YNL008C	ASI3	Class 2
YNL010W	PYP1	Class 2
YNR047W	FPK1	Class 2
YBR027C		Class 2
YBR043C	QDR3	Class 2
YML036W	CGI121	Class 2
YPL004C	LSP1	Class 2
YML066C	SMA2	Class 2
YBR133C	HSL7	Class 2
YDL002C	NHP10	Class 2

YBR172C	SMY2	Class 2
YDL021W	GPM2	Class 2
YDR462W	MRPL28	Class 2
YDR500C	RPL37B	Class 2
YGL136C	MRM2	Class 2
YER174C	GRX4	Class 2
YER167W	BCK2	Class 2
YMR221C	FMP42	Class 2
YIL094C	LYS12	Class 2
YGR254W	ENO1	Class 2
YMR257C	PET111	Class 2
YMR278W	PRM15	Class 2
YMR291W	TDA1	Class 2
YMR303C	ADH2	Class 2
YNL303W		Class 2
YNL302C	RPS19B	Class 2
YNL265C	IST1	Class 2
YNL264C	PDR17	Class 2

Table S2: List of yeast strains and plasmids

Strain ID	Genotype	Source	
BY4741	*MATa his3Δ1; leu2Δ0; met15Δ0; ura3Δ0*		
RLY8616	*GRX5-GFP$_{11}$-His3MX6; trp1::P$_{GPD}$-MTS-mCherry-GFP$_{1-10}$-natMX6*	Ruan, L. et al., 2017.	
RLY8618	*LSG1-GFP$_{11}$-His3MX6; trp1::P$_{GPD}$-MTS-mCherry-GFP$_{1-10}$-natMX6*	Ruan, L. et al., 2017.	
RLY9798	*LSG1-GFP$_{11}$-His3MX6; trp1::P$_{GPD}$-MTS-mCherry-GFP$_{1-10}$-natMX6; Δsnf1::kanMX6*	This study	
RLY9799	*LSG1-GFP$_{11}$-His3MX6; trp1::P$_{GPD}$-MTS-mCherry-GFP$_{1-10}$-natMX6; Δltv1::kanMX6*	This study	
RLY9800	*ura3Δ0::GEM-hphMX6; trp1::P$_{GPD}$-GRX5-HA-GFP$_{1-10}$-natMX6; HO::P$_{GAL1}$-FlucSM-HA-GFP$_{11}$-His3MX6; TOM70-mCherry-Ura3MX6*	This study	
RLY9801	*ura3Δ0::GEM-hphMX6; trp1::P$_{GPD}$-GRX5-HA-GFP$_{1-10}$-natMX6; HO::P$_{GAL1}$-FlucSM-HA-GFP$_{11}$-His3MX6; TOM70-mCherry-Ura3MX6; Δreg1::Leu2*	This study	
RLY9802	*trp1::P$_{GPD}$-GRX5-HA-GFP$_{1-10}$-natMX6; amp::GEM-P$_{GAL1}$-FlucSM-HA-GFP$_{11}$-kanMX6; TOM70-RFP-hphMX6*	This study	
RLY9803	*trp1::P$_{GPD}$-GRX5-HA-GFP$_{1-10}$-natMX6; amp::GEM-P$_{GAL1}$-FlucSM-HA-GFP$_{11}$-kanMX6; TOM70-mCherry-Ura3MX6*	This study	
RLY9804	*trp1::P$_{GPD}$-GRX5-HA-GFP$_{1-10}$-natMX6; amp::GEM-P$_{GAL1}$-FlucWT-HA-GFP$_{11}$-kanMX6; TOM70-mCherry-Ura3MX6*	This study	
RLY9805	*trp1::P$_{GPD}$-GRX5-HA-GFP$_{1-10}$-natMX6; amp::GEM-P$_{GAL1}$-FlucDM-HA-GFP$_{11}$-kanMX6; TOM70-mCherry-Ura3MX6*	This study	
RLY9806	*MIG1-GFP-His3MX6; PUS1-RFP-hphMX6*	This study	
RLY9807	*MIG1-GFP-His3MX6; PUS1-RFP-hphMX6; Δreg1::Leu2*	This study	
RLY9808	*ura3Δ0::P$_{CUP1}$-PIM1-Ura3; GRX5-GFP$_{1-10}$-natMX6; trp1::P$_{GPD}$-mCherry-Fis1TM-hphMX6; amp::GEM-P$_{GAL1}$-FlucSM-HA-GFP$_{11}$-kanMX6*	This study	
RLY9809	*ura3Δ0::P$_{CUP1}$-pim1^{S974D}-Ura3; GRX5-GFP$_{1-10}$-natMX6; trp1::P$_{GPD}$-mCherry-Fis1TM-hphMX6; amp::GEM-P$_{GAL1}$-FlucSM-HA-GFP$_{11}$-kanMX6*	This study	
RLY9810	*trp1::P$_{GPD}$-MTS-mCherry-natMX6; amp::GEM-P$_{GAL1}$-FlucSM-HA-GFP$_{11}$-kanMX6*	This study	
RLY9811	*trp1::P$_{GPD}$-MTS-mCherry-natMX6; amp::GEM-P$_{GAL1}$-FlucSM-HA-GFP$_{11}$-kanMX6; Δreg1::His3MX6*	This study	
RLY9812	*ura3Δ0::GEM-hphMX6; trp1::P$_{GPD}$-GRX5-HA-GFP$_{1-10}$-natMX6; HO::P$_{GAL1}$-FlucSM-HA-GFP$_{11}$-His3MX6; TOM70-mCherry-Ura3MX6; Δreg1::Leu2; Δhap4::kanMX6*	This study	
RLY9813	*trp1::P$_{GPD}$-GRX5-HA-GFP$_{1-10}$-natMX6; amp::GEM-P$_{GAL1}$-FlucSM-HA-GFP$_{11}$-kanMX6;*	This study	

	TOM70-mCherry-Ura3MX6; HO::P_{GPD}-HAP4-hphMX6		
RLY9814	*ura3Δ0::GEM-hphMX6; trp1::P_{GPD}-GRX5-HA-GFP_{1-10}-natMX6; HO::P_{GAL1}-FlucSM-HA-GFP_{11}-His3MX6; TOM70-mCherry-Ura3MX6; Δatg1::kanMX6*	This study	
RLY9815	*ura3Δ0::GEM-hphMX6; trp1::P_{GPD}-GRX5-HA-GFP_{1-10}-natMX6; HO::P_{GAL1}-FlucSM-HA-GFP_{11}-His3MX6; TOM70-mCherry-Ura3MX6; Δatg15::kanMX6*	This study	
RLY9816	*ura3Δ0::GEM-hphMX6; trp1::P_{GPD}-GRX5-HA-GFP_{1-10}-natMX6; HO::P_{GAL1}-FlucSM-HA-GFP_{11}-His3MX6; TOM70-mCherry-Ura3MX6; Δmig1::kanMX6*	This study	
RLY9817	*ura3Δ0::GEM-hphMX6; trp1::P_{GPD}-GRX5-HA-GFP_{1-10}-natMX6; HO::P_{GAL1}-FlucSM-HA-GFP_{11}-His3MX6; TOM70-mCherry-Ura3MX6; Δmig2::Leu2*	This study	
RLY9818	*ura3Δ0::GEM-hphMX6; trp1::P_{GPD}-GRX5-HA-GFP_{1-10}-natMX6; HO::P_{GAL1}-FlucSM-HA-GFP_{11}-His3MX6; TOM70-mCherry-Ura3MX6; Δmig1::kanMX6; Δmig2::Leu2*	This study	
RLY9819	*ura3Δ0::GEM-hphMX6; trp1::P_{GPD}-GRX5-HA-GFP1-10-natMX6; HO::PGAL1-FlucSM-HA-GFP11-His3MX6; TOM70-mCherry-Ura3MX6; Δreg1::Leu2; Δcat8::kanMX6*	This study	
RLY9820	*ura3Δ0::GEM-hphMX6; trp1::P_{GPD}-GRX5-HA-GFP1-10-natMX6; HO::PGAL1-FlucSM-HA-GFP11-His3MX6; TOM70-mCherry-Ura3MX6; Δreg1::Leu2; Δsip4::kanMX6*	This study	
RLY9821	*ura3Δ0::GEM-hphMX6; trp1::P_{GPD}-GRX5-HA-GFP1-10-natMX6; HO::PGAL1-FlucSM-HA-GFP11-His3MX6; TOM70-mCherry-Ura3MX6; Δreg1::Leu2; Δrds2::kanMX6*	This study	
RLY9822	*ura3Δ0::GEM-hphMX6; trp1::P_{GPD}-GRX5-HA-GFP1-10-natMX6; HO::PGAL1-FlucSM-HA-GFP11-His3MX6; TOM70-mCherry-Ura3MX6; Δreg1::Leu2; Δadr1::kanMX6*	This study	
RLY9823	*trp1::P_{GPD}-GRX5-HA-GFP_{1-10}-natMX6; amp::GEM-P_{GAL1}-FlucSM-HA-GFP_{11}-kanMX6; TOM70-mCherry-Ura3MX6; HO::P_{GPD}-$tom20_{cd}$-hphMX6*	This study	
RLY9824	*trp1::P_{GPD}-GRX5-HA-GFP_{1-10}-natMX6; amp::GEM-P_{GAL1}-FlucSM-HA-GFP_{11}-kanMX6; TOM70-mCherry-Ura3MX6; HO::P_{GPD}-$tom22_{cd}$-hphMX6*	This study	
RLY9825	*ura3Δ0::GEM-hphMX6; trp1::P_{GPD}-GRX5-HA-GFP_{1-10}-natMX6; HO::P_{GAL1}-FlucSM-HA-GFP_{11}-His3MX6; TOM70-mCherry-Ura3MX6; amp::P_{GPD}-$tom70_{cd}$-3xFLAG-kanMX6*	This study	

RLY9826	*ura3Δ0::GEM-hphMX6; trp1::P_{GPD}-GRX5-HA-GFP_{1-10}-natMX6; HO::P_{GAL1}-FlucSM-HA-GFP_{11}-His3MX6; TOM70-mCherry-Ura3MX6; amp::P_{GPD}-$tom70_{cd}$(Δ98-214)-3xFLAG-kanMX6*	This study	
RLY9827	*ura3Δ0::GEM-hphMX6; trp1::P_{GPD}-GRX5-HA-GFP_{1-10}-natMX6; HO::P_{GAL1}-FlucSM-HA-GFP_{11}-His3MX6; TOM70-mCherry-Ura3MX6; amp::P_{GPD}-$tom70_{cd}$(Δ247-617)-3xFLAG-kanMX6*	This study	
RLY9828	*ura3Δ0::GEM-hphMX6; trp1::P_{GPD}-GRX5-HA-GFP_{1-10}-natMX6; HO::P_{GAL1}-FlucSM-HA-GFP_{11}-His3MX6; trp1::P_{GPD}-mCherry-Fis1TM-kanMX6*	This study	
RLY9829	*ura3Δ0::GEM-hphMX6; trp1::P_{GPD}-GRX5-HA-GFP_{1-10}-natMX6; HO::P_{GAL1}-FlucSM-HA-GFP_{11}-His3MX6; trp1::P_{GPD}-mCherry-Fis1TM-kanMX6; Δtom70::Ura3MX6*	This study	
RLY9830	*ura3Δ0::GEM-hphMX6; trp1::P_{GPD}-GRX5-HA-GFP_{1-10}-natMX6; HO::P_{GAL1}-FlucSM-HA-GFP_{11}-His3MX6; trp1::P_{GPD}-mCherry-Fis1TM-kanMX6; Δtom71::Leu2*	This study	
RLY9831	*ura3Δ0::GEM-hphMX6; trp1::P_{GPD}-GRX5-HA-GFP_{1-10}-natMX6; HO::P_{GAL1}-FlucSM-HA-GFP_{11}-His3MX6; trp1::P_{GPD}-mCherry-Fis1TM-kanMX6; Δtom70::Ura3MX6; Δtom71::Leu2*	This study	
RLY9832	*ura3Δ0::GEM-hphMX6; trp1::P_{GPD}-GRX5-HA-GFP_{1-10}-natMX6; HO::P_{GAL1}-FlucSM-HA-GFP_{11}-His3MX6; TOM70-mCherry-Ura3MX6; amp::P_{GPD}-$tom70_{cd}$-3xFLAG-kanMX6; Δtom6::Leu2*	This study	
RLY9833	*ura3Δ0::GEM-hphMX6; trp1::P_{GPD}-GRX5-HA-GFP_{1-10}-natMX6; HO::P_{GAL1}-FlucSM-HA-GFP_{11}-His3MX6*	This study	
RLY9834	*ura3Δ0::GEM-hphMX6; trp1::P_{GPD}-GRX5-HA-GFP_{1-10}-natMX6; HO::P_{GAL1}-FlucSM-HA-GFP_{11}-His3MX6; amp::P_{GPD}-$tom70_{cd}$-3xFLAG-kanMX6*	This study	
RLY9835	*ura3Δ0::P_{GPD}-a-Synuclein-HA-GFP_{11}-His3MX6; GRX5-GFP_{1-10}-natMX6; TOM70-mCherry-Ura3MX6*	This study	
RLY9836	*ura3Δ0::P_{GPD}-a-Synuclein-HA-GFP_{11}-His3MX6; GRX5-GFP_{1-10}-natMX6; TOM70-mCherry-Ura3MX6; Δreg1::Leu2*	This study	
RLY9837	*ura3Δ0::P_{GPD}-a-Synuclein-HA-GFP11-His3MX6; GRX5-GFP1-10-natMX6; TOM70-mCherry-Ura3MX6; trp1::P_{GPD}-$tom70_{cd}$-3xFLAG-kanMX6*	This study	
RLY9838	*ura3Δ0::P_{GPD}-a-Synuclein-HA-GFP_{11}-His3MX6; GRX5-GFP_{1-10}-natMX6*	This study	
RLY9839	*ura3Δ0::P_{GPD}-a-Synuclein-HA-GFP11-His3MX6; GRX5-GFP1-10-natMX6; trp1::P_{GPD}-$tom70_{cd}$-3xFLAG-kanMX6*	This study	

RLY9840	*trp1::P_{GPD}-GRX5-HA-GFP$_{1-10}$-natMX6; TOM70-mCherry-Ura3MX6; amp::GEM-P_{GAL1}-FUS^{P525L}-HA-GFP$_{11}$-kanMX6*	This study	
RLY9841	*ura3Δ0::GEM-hphMX6; trp1::P_{GPD}-GRX5-HA-GFP$_{1-10}$-natMX6; HO::P_{GAL1}-FUS^{P525L}-HA-GFP$_{11}$-His3MX6; TOM70-mCherry-Ura3MX6*	This study	
RLY9842	*ura3Δ0::GEM-hphMX6; trp1::P_{GPD}-GRX5-HA-GFP$_{1-10}$-natMX6; HO::P_{GAL1}-FUS^{P525L}-HA-GFP$_{11}$-His3MX6; TOM70-mCherry-Ura3MX6; Δreg1::Leu2*	This study	
RLY9843	*ura3Δ0::GEM-hphMX6; trp1::P_{GPD}-GRX5-HA-GFP$_{1-10}$-natMX6; HO::P_{GAL1}-FUS^{P525L}-HA-GFP$_{11}$-His3MX6; TOM70-mCherry-Ura3MX6; amp::P_{GPD}-tom70$_{cd}$-3xFLAG-kanMX6*	This study	
RLY9844	*trp1::P_{GPD}-GRX5-HA-GFP$_{1-10}$-natMX6; amp::GEM-P_{GAL1}-FUS^{P525L}-HA-GFP$_{11}$-kanMX6*	This study	
RLY9845	*trp1::P_{GPD}-GRX5-HA-GFP$_{1-10}$-natMX6; amp::GEM-P_{GAL1}-FUS^{P525L}-HA-GFP$_{11}$-kanMX6; trp1::P_{GPD}-tom70$_{cd}$-3xFLAG-kanMX6*	This study	
RLY9846	*ura3Δ0::GEM-hphMX6; trp1::P_{GPD}-GRX5-HA-GFP$_{1-10}$-natMX6; HO::P_{GAL1}-FlucSM-HA-GFP$_{11}$-His3MX6; TOM70-mCherry-Ura3MX6; Δpdr5::kanMX6*	This study	
RLY9847	*ura3Δ0::GEM-hphMX6; trp1::P_{GPD}-GRX5-HA-GFP$_{1-10}$-natMX6; HO::P_{GAL1}-FlucSM-HA-GFP$_{11}$-His3MX6; TOM70-mCherry-Ura3MX6; Δhap4::kanMX6*	This study	

Plasmid ID	**Construct**	**Vector type**	**Source**
RLB918	*TRP1::P_{GPD}-MTS-mCherry-GFP$_{1-10}$-natMX6*	Yeast expression	Ruan, L. et al., 2017.
RLB919	*TRP1::P_{GPD}-Grx5-HA-GFP$_{1-10}$-natMX6*	Yeast expression	Ruan, L. et al., 2017.
pJW1663	*GEM-P_{GAL1}-GFP-kanMX6*	Yeast expression	Costa, E.A. et al. 2018.
RLB1050	*TRP1::P_{GPD}-mCherry-Fis1TM-KanMX6*	Yeast expression	Ruan, L. et al., 2017.
RLB1051	*GEM-P_{GAL1}-FlucSM-HA-GFP$_{11}$-KanMX6*	Yeast expression	This study
RLB1052	*GEM-P_{GAL1}-FlucWT-HA-GFP$_{11}$-KanMX6*	Yeast expression	This study
RLB1053	*GEM-P_{GAL1}-FlucDM-HA-GFP$_{11}$-KanMX6*	Yeast expression	This study
RLB1054	*GEM-P_{GAL1}-FUS^{P525L}-HA-GFP$_{11}$-KanMX6*	Yeast expression	This study
RLB1055	*pRS316-P_{CUP1}-PIM1-Ura3*	Yeast expression	Nitika et al. 2022
RLB1056	*pRS316-P_{CUP1}-pim1^{S974D}-Ura3*	Yeast expression	Nitika et al. 2022

RLB1057	*pRS313-HO(homology)-P_{GAL1}-FlucSM-HA-GFP_{11}-His3MX6-HO(homology)*	Yeast expression	This study
RLB1058	*pRS313-HO(homology)-P_{GAL1}-FUS^{P525L}-HA-GFP_{11}-His3MX6-HO(homology)*	Yeast expression	This study
RLB1059	*pRS316-HO(homology)-P_{GPD}-HAP4-hphMX6-HO(homology)*	Yeast expression	This study
RLB1060	*TRP1::P_{GPD}-$tom70_{cd}$-3xFLAG-KanMX6*	Yeast expression	This study
RLB1061	*TRP1::P_{GPD}-$tom70_{cd}$(Δ98-214)-3xFLAG-KanMX6*	Yeast expression	This study
RLB1062	*TRP1::P_{GPD}-$tom70_{cd}$(Δ247-617)-3xFLAG-KanMX6*	Yeast expression	This study
RLB1063	*pRS316-HO(homology)-P_{GPD}-$tom20_{cd}$-hphMX6-HO(homology)*	Yeast expression	This study
RLB1064	*pRS316-HO(homology)-P_{GPD}-$tom22_{cd}$-hphMX6-HO(homology)*	Yeast expression	This study
RLB1065	*P_{GPD}-a-Synuclein-HA-GFP_{11}-His3MX6*	Yeast expression	This study
RLB1066	*P_{CMV}-FUS^{P525L}-HA-GFP_{11}*	Mammalian expression	Ruan, L. et al., 2017.
RLB912	*P_{CMV}-MTS-mCherry-GFP_{1-10}*	Mammalian expression	Ruan, L. et al., 2017.
RLB914	*P_{CMV}-FlucDM-HA-GFP_{11}*	Mammalian expression	Ruan, L. et al., 2017.
RLB916	*P_{CMV}-GST-HA-GFP_{11}*	Mammalian expression	Ruan, L. et al., 2017.